ADVANCED COOLING TECHNOLOGIES, INC.

Innovations in Action

ISO9001 & AS9100
Certified

CONTRACT NO. DE-SC0004729

ACT PROJECT NO. TD0095RD

**SYNGAS PRODUCTION BY THERMOCHEMICAL CONVERSION OF
H_2O AND CO_2 MIXTURES USING A NOVEL REACTOR DESIGN**

FINAL REPORT

PERIOD COVERED: August 15, 2011 through December 31, 2013

PREPARED FOR:

Mr. Douglas B. Archer
Office of Fossil Energy FE-224
U.S. Department of Energy
Washington, DC 20585

PREPARED BY:

Chien-Hua Chen, Ph.D.
Advanced Cooling Technologies, Inc.
R&D Engineer
Technology Development Group
Chien-Hua.Chen@1-act.com
717-295-6116

Howard Pearlman, Ph.D. (PI)
Advanced Cooling Technologies, Inc.
Manager
Technology Development Group
Howard.Pearlman@1-act.com
717-295-6815

With input provided by Professor Haile at CalTech and
Dr. Richard Diver of Diver Solar LLC

APPROVED BY:

_____

Jon Zuo, Chief Technical Officer

December 31, 2013 (revised/ updated August 27, 2014)

Table of Contents

1. Executive Summary

The Department of Energy awarded Advanced Cooling Technologies, Inc. (ACT) an SBIR Phase II contract (#DE-SC0004729) to develop a high-temperature solar thermochemical reactor for syngas production using water and/or carbon dioxide as feedstocks. The technology aims to provide a renewable and sustainable alternative to fossil fuels, promote energy independence and mitigate adverse issues associated with climate change by essentially recycling carbon from carbon dioxide emitted by the combustion of hydrocarbon fuels. To commercialize the technology and drive down the cost of solar fuels, new advances are needed in materials development and reactor design, both of which are integral elements in this program.

Regarding the reactor design, ACT leveraged our expertise with high-temperature materials and heat pipes and worked closely with DiverSolar LLC to assess different heat pipe-based solar receiver/reactor designs. In contrast to other reactor designs, a heat pipe based reactor offers the ability to efficiently collect and transfer concentrated solar energy to the working material where it can be used for fuel production. Heat loss due to re-radiation can also be minimized thus increasing the overall conversion efficiency (solar to fuel).

For materials development and screening, ACT partnered with Professor Haile and her team at California Institute of Technology (CIT). Their role was to identify and screen candidate materials that can be thermally reduced at comparatively low temperatures while having appropriate thermodynamics and sufficiently fast kinetics associated with the re-oxidation of reduced metal oxides using CO_2 and/or H_2O. CIT results showed zirconium (Zr) substituted cerium oxide can in fact lower the temperature for the thermal reduction half cycle, the most challenging issue for two-step metal oxide based thermochemical cycles. While the temperature for thermal reduction (compared to pure ceria) can be reduced, a minimum temperature of $1300^{o}C$ is still needed. Also, CIT evaluated praseodymium (Pr) as a new potential dopant to replace Zr. Praseodymium oxide itself has a large oxygen non-stoichiometry at reasonably low temperature ($< 1000^{o}C$), yet reduced praseodymium oxide has insufficient reducing power to reduce H_2O or CO_2 needed to generate H_2 or CO. However, the results of Pr doped ceria show significant conversion efficiency improvement at $1300^{o}C$.

Based on the CIT results showing the reactor must be operate at $1300^{o}C$ or higher needed for reduction of the oxide, ACT focused on a reactor design made from refractory metals rather than nickel-based superalloys that suffer from undesirable issues with thermal creep. Refractory metals can handle extremely high temperatures, yet require advanced machining/ welding techniques, are somewhat expensive and are highly susceptible to oxidation at elevated temperature. To suppress oxidation, ACT's heat pipe based reactor, which was based on a lithium-filled molybdenum (TZM) alloy heat pipe, was designed to operate in a vacuum. The heat pipe was successfully built and tested in a vacuum environment. Furthermore, in our design, the heat pipe was radiatively coupled to the reactor assembly containing the working material (metal oxide).

In parallel with the development of the high-temperature refractory metal heat pipe based reactor, ACT together with Dr. Diver from DiverSolar LLC and Rowan University also explored a new multistep thermochemical cycle that is thermodynamically feasible and requires a maximum temperature less than $1000^{o}C$. This temperature range is very attractive since inexpensive, readily available materials can be used for the reactor housing and solar heat as well as nuclear heat can be used for driving the endothermic reactions. Thermodynamic analyses and results from flow reactor studies are presented herein. Interestingly, three of the four proposed steps are standard, commercial processes and only one new step is required to close the cycle such that the net reaction is that for water or carbon dioxide splitting. Note also that a patent on the process has been filed to protect the intellectual property. Lastly, recommendations for future work are also discussed based on lessons learned in this program.

2. Background

Energy sustainability and climate change are two major challenges in the 21st century. One proposed renewable energy strategy to address both concerns involves the use of a thermochemical cycle to convert CO_2 and H_2O to CO and H_2 (syngas) using concentrated solar energy to drive the endothermic reduction portion of the cycle. The process works by cyclically changing the thermodynamic state of the working material(s) to convert the thermal energy to chemical energy. Several reactions may be involved but the overall reaction reduces to water or CO_2 splitting. The produced syngas can subsequently be converted into liquid fuels using the Fischer-Tropsch process or used to synthesize chemicals and other materials [1].

Early work on water splitting thermochemical cycles aimed to use nuclear reactors, rather than solar thermal energy, to provide the heat input to the cycle. These cycles often involve several steps and a maximum temperature of $\approx 750 \sim 850^{o}C$, yet have challenging separation processes. Several hundred thermochemical cycles have been identified in the past 30 ~ 40 years and detailed screening of the cycles based on the number of reaction steps, operating temperatures, cycle efficiency, etc. has been studied [2]. Alternatively, simple two-step cycle can also be achieved using metal oxides yet they require higher reduction temperatures ($\sim 1500^{o}C$) that can be provided by concentrated solar power (CSP). Several metal oxides have been studied for use in two-step processes with a focus on iron oxide (Fe_3O_4/FeO) and zinc oxide (ZnO/Zn). The higher temperature requirement for two-step cycles however introduces other practical challenges regarding the stability of working material and operating temperature of the structural materials. To address materials issues, researchers have been actively screening candidate materials and evaluating options to lower the reduction temperature while maintaining the simplicity of the two-step cycle.

While most efforts focus on the materials development, the overall solar-to-fuel efficiency of the process is also highly dependent on the effectiveness of the heat transfer process [3]. It is important that the solar thermal energy is transferred to the material and not lost or re-radiated (effectively a loss). In this work, a simple analysis of the heat transfer in the solar reactor is therefore addressed. Based on this work, a heat pipe based reactor was developed to enhance the heat transfer of the concentrated solar power into the metal oxide material. Leveraging ACT's experience with heat pipes, a system has been developed to perform a two-step thermal cycle without the need for moving parts.
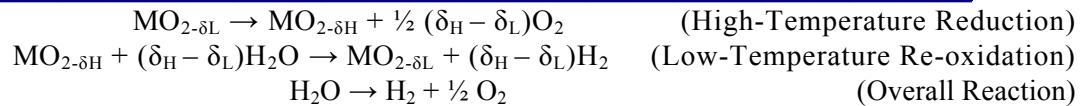
2-1. Two-step Metal Oxide Based Thermochemical Cycles

The production of fuels from two-step thermochemical cycling of metal oxides occurs by: (1) thermal reduction of the metal oxide at high temperatures, which generates oxygen; and (2) re-oxidation of the metal oxide at lower temperatures by steam and/or carbon dioxide, which produces the chemical fuel (Figure 2-1).
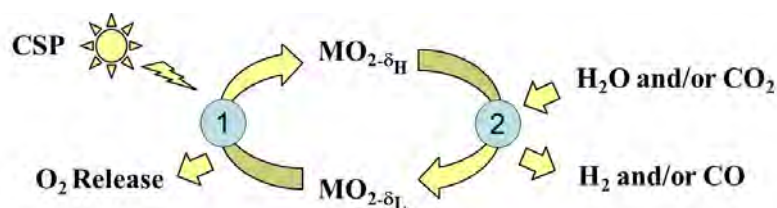
Figure 2-1. Two-step solar thermochemical cycle. Metal oxide (MO_2) is thermally reduced at high temperature (step 1) and re-oxidized by H_2O and/or CO_2 to produce H_2 and/or CO (step 2).

The thermochemical reactions for the production of hydrogen, specific to a metal oxide with variable oxygen content, can be written in the following form:

$$MO_{2-\delta_L} \rightarrow MO_{2-\delta_H} + \tfrac{1}{2}(\delta_H - \delta_L)O_2 \qquad \text{(High-Temperature Reduction)}$$
$$MO_{2-\delta_H} + (\delta_H - \delta_L)H_2O \rightarrow MO_{2-\delta_L} + (\delta_H - \delta_L)H_2 \quad \text{(Low-Temperature Re-oxidation)}$$
$$H_2O \rightarrow H_2 + \tfrac{1}{2}O_2 \qquad \text{(Overall Reaction)}$$

where MO represents a metal oxide, M is the metal of variable oxidation state (with dopant(s)), and δ_H and δ_L are the high and low temperature oxygen nonstoichiometry values relative to an ideal structure with stoichiometry MO_2. The difference between δ_H and δ_L ($\Delta\delta$) directly corresponds to the quantity of fuel produced in each cycle.

The thermal reduction step involving oxygen release is critically dependent on the temperature and oxygen partial pressure. For typical metal oxides, temperatures in the range of 1400^oC to 1600^oC (in an inert gas environment, $P_{O2} \approx 10^{-5} \sim 10^{-6}$ atm) are required with associated nonstoichiometries (δ) on the order of 0.10 [4, 5]. For the fuel production step, the amount of hydrogen gas produced is directly related to the amount of oxygen removed in the thermal reduction step.

Whether a particular reduced metal oxide is suitable for subsequent H_2O and/or CO_2 dissociation depends on both thermodynamic and kinetic factors. Specifically, the thermodynamics must be such that the reduced metal oxide has sufficient reducing power to drive the dissociation reaction. Furthermore, the oxygen must diffuse through the reduced metal oxide material at a sufficiently fast rate during the thermal reduction half-cycle and the kinetics must be sufficiently fast during the re-oxidation (dissociation) half cycle. Recently, ceria based material has attracted attention. The ceria cycle is conceptually similar to that of other metal oxides, but differs in that the reduced and oxidized states do not correspond to distinct phases (in contrast to other cycles, e.g., the ferrite cycle FeO/Fe_3O_4). Accordingly, the extent of reduction or equivalently the stoichiometry change can be of arbitrary value. The advantages of ceria based material are fast reduction and re-oxidation rates, it is a good oxygen ion conductor, has a high O_2 diffusion rate, has no phase change at high temperature, and has no carbon deposit in the low-temperature re-oxidation step. While there are several advantages of the ceria based cycle, the temperature requirement for thermal reduction step is still very high (> 1400^oC). This poses a significant challenge for the structural materials as the reactor design must handle the high temperatures and temperature swing. In addition, the low thermal conductivity of the porous metal oxide limits the extent to which the material is reduced during the thermal reduction half cycle (as it is heated by the high heat flux from the concentrated). These challenges need to be overcome to realize high efficiencies with solar-to-fuel conversion via the two-step ceria based thermochemical cycle.

Heat Transfer Analysis
Unlike other water or carbon dioxide splitting methods, such as electrolysis or photoelectrochemical processes, the thermochemical cycle involves the conversion of thermal energy into chemical potential. The attainable efficiency of the cycle is governed by the second law of thermodynamics and is affected by how efficiently heat is transferred into and out of the material. In addition, the cyclic nature of the process makes the system transient rather than steady-state. Figure 2-2A shows the thermal energy flow for a representative thermochemical cycle. The thermal energy is collected and absorbed by the (solar) receiver, then transferred to the reactor structure then re-radiated to the environment or taken up by the working material; the distribution of thermal energy depends on the relative magnitude of the thermal resistances (Figure 2-2B). Clearly, to maximize the system efficiency, most of the thermal energy should be used to heat the metal oxide material and the heat lost to the environment or used to heat the reactor structure minimized. Therefore, the overall goal of our thermal design was to minimize the thermal resistance of the metal oxide material.
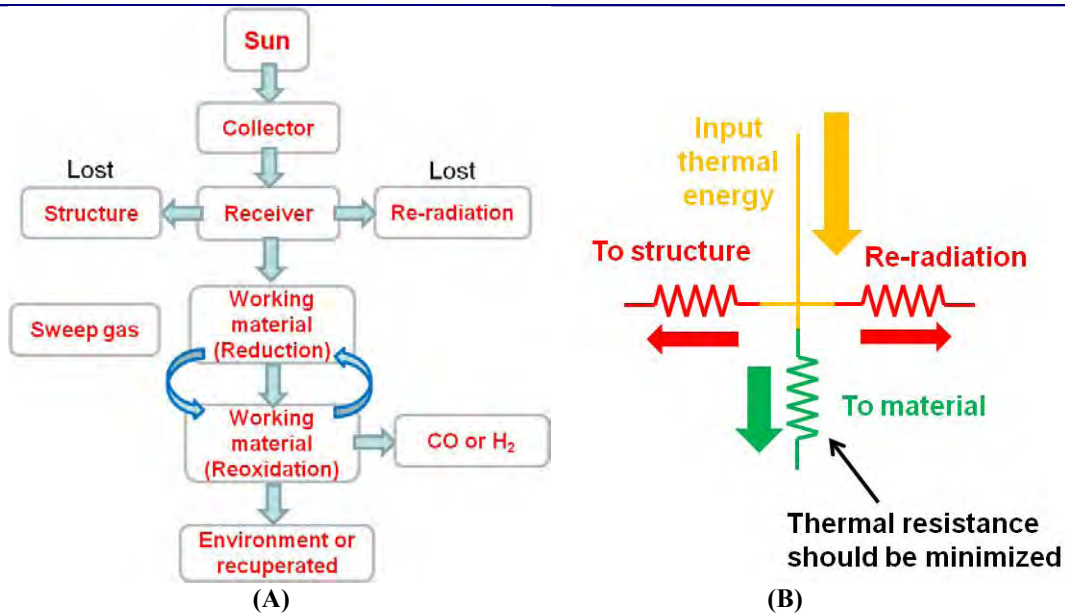
Figure 2-2. (A) Thermal energy flow analysis for a thermochemical cycle. The heat absorbed by the solar receiver is used to heat the structural material, re-radiated to the environment, or transferred to the metal oxide material. The thermal resistance between receiver and working material should be minimized to maximize the heat transfer into the material and thus maximize the solar to fuel efficiency. (B) The thermal resistance chart. The portion of overall thermal energy transferred to the material is determined by the relative magnitude of the thermal resistances.

For a fixed bed type reactor design [6], the dominant thermal resistance is the conduction resistance into the material (Figure 2-3A) since the porous ceria-based material has a very low thermal conductivity. For example, the effective thermal conductivity (k) of porous ceria with 80% porosity is less than 0.1 W/m·K (with an Ar sweep gas). The associated high thermal resistance of the material results in the surface of the material being heated very rapidly and a steep temperature gradient through the material. At high temperature, the re-radiation resistance is low such that most of the thermal energy re-radiates back to the environment rather than conducting into the material to thermally reduce it. In turn, this limits/ lowers the fuel productivity. To lower the conduction resistance and reduce more of the material (thus produce more fuel), the material thickness (L) can be decreased and/or the heat transfer area (A_m) increased. At the same time, there is an additional requirement on the amount of material needed to reduce a sufficient amount of H_2O or CO_2 to generate H_2 or CO and achieve the theoretical efficiency; as such, the amount of material cannot simply be reduced in order to reduce the thickness of the layer (thermal resistance). Rather, the material must be distributed in a thin layer and the heat transfer area should be increased such that a given amount of material can be rapidly heated and thermally reduced.

On the other hand, for a moving bed type reactor design [7, 8], a similar thermal analysis can be done. In this configuration, a thin layer of material is typically placed on a large rotating wheel. In this case, the dominant thermal resistance depends on the thermal mass flow (Figure 2-3B), which in turn depends on the rotation rate of the wheel. While the conduction resistance may not be large for a reactor with a thin metal oxide layer, other factors including the chemical time for re-oxidation must be factored in to optimize the system efficiency. For example, the rotation speed may not be limited by the reduction thermal time scale, but rather by the re-oxidation chemical time scale, which depends on the kinetics. Clearly, to maximize the system level efficiency, both thermal and chemical time scales for the reduction and re-oxidation steps would ideally be balanced such that the moving bed can operate at a fixed rotation speed.

(A)   (B)
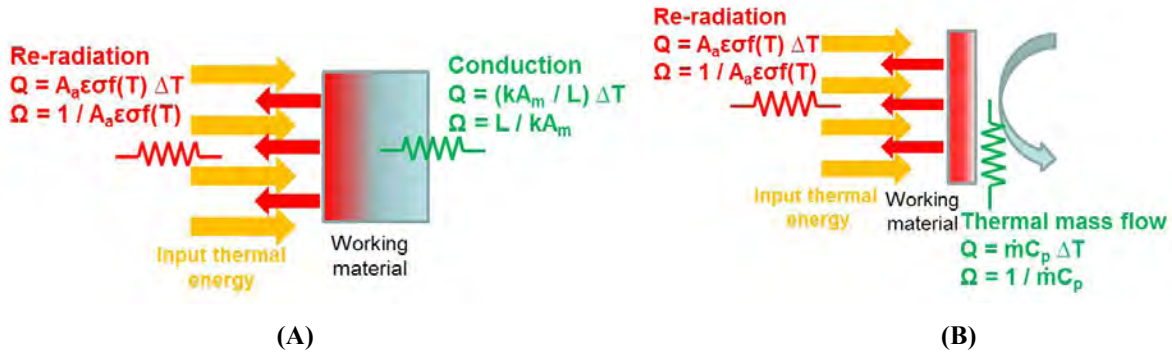
Figure 2-3. Schematic of dominant thermal resistances. (A) Fixed bed type reactor. In re-radiation heat transfer (heat loss), A_a is the receiver aperture area, which is a function of material surface temperature. In conduction heat transfer, A_m is the heat transfer area of the material, k is the material thermal conductivity, and L is the material thickness. (B) Moving bed type reactor. Assuming conduction to the working material is not the dominant thermal resistance, the thermal resistance of the thermal mass flow (depending on the rotation rate of the material) will dominate.

The effect of increasing heat transfer area on thermal energy usage improvement can be explained by the following example. For a material with thickness 1 cm and 80% porosity, even if the heat transfer area (A_m) is 10 times that of the aperture area A_a (for typical cavity receiver), for a material surface temperature of 1000K, the thermal resistance of re-radiation (red line in Figure 2-4) is equal to that associated with that for conduction to the material (solid green line in Figure 2-4, $\Omega_{rad}A_a = \Omega_{cond}A_a \rightarrow \Omega_{rad} = \Omega_{cond}$ for $A_m/A_a = 10$ at 1000K), which means at least half of the input thermal energy will re-radiate back to the environment. Clearly, by further increasing A_m/A_a ratio, a relatively small conduction thermal resistance can be achieved (dash lines in Figure 2-4) so that more input thermal energy will be transferred into the working material. This can be achieved by the proposed heat pipe based reactor as described in the next section.
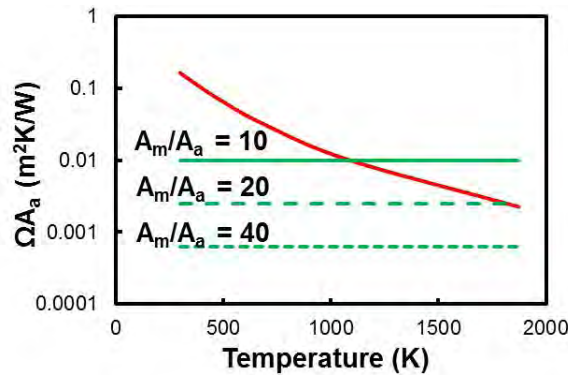
Figure 2-4. Thermal resistance of re-radiation (red line) and conduction (green lines) vs. temperature.

*Second Law Analysis of Thermochemical Cycle*

The thermodynamics of heat engines is useful for the determination of energy flows and for calculating efficiency, routine for conventional heat engines such as steam cycle power plants and gas turbines. However, the cerium oxide thermochemical cycle is different from conventional heat engines in that its output is in the form of chemical potential rather than mechanical work. However, thermodynamically they are governed by the same principles. Just like in conventional thermodynamic cycles, temperature-entropy (T-s) diagrams are useful for illustrating how high-temperature heat is converted into useful work and quantifying the energy flows and temperatures needed to make them work.

The two chemical reactions in the cerium oxide cycle are:

$$CeO_2 \rightarrow \tfrac{1}{2}\, Ce_2O_3 + \tfrac{1}{4}\, O_2 \qquad \text{(Reaction 1)}$$
$$\tfrac{1}{2}\, Ce_2O_3 + \tfrac{1}{2}\, H_2O \rightarrow CeO_2 + \tfrac{1}{2}\, H_2 \qquad \text{(Reaction 2)}$$

Reaction 1 is the thermal reduction of cerium oxide to produce oxygen and occurs at the high temperature, T_H. In reaction 2, the reduced cerium oxide is re-oxidized with water, producing hydrogen, and occurs at the low temperature, T_L.

Figure 2-5 is a T-s diagram illustrating the idealized steps in the cerium oxide thermochemical cycle. The numbers in the T-s diagram illustrate state points in the thermochemical cycle and the enclosed solid blue color area represents the chemical work output per cycle. Point 1 is the start of the cycle with CeO_2 at T_L. The CeO_2 is then heated to T_H, point 2. In the high-temperature, endothermic, thermal-reduction reaction additional heat is added isothermally and oxygen is produced, point 3. Removing the oxygen reduces the entropy of the system leaving the reduced cerium oxide in state 4. Heat rejection cools the reduced cerium oxide to T_L, state 5. Introducing water vapor increases the system entropy to point 6. The exothermic, low-temperature, oxidation reaction re-oxidizes the cerium oxide to CeO_2 and produces hydrogen at step 7. Removal of the hydrogen completes the cycles leaving CeO_2 at state 1. The use of T-s diagram to analyze the thermochemical cycle was also discussed in reference [9].
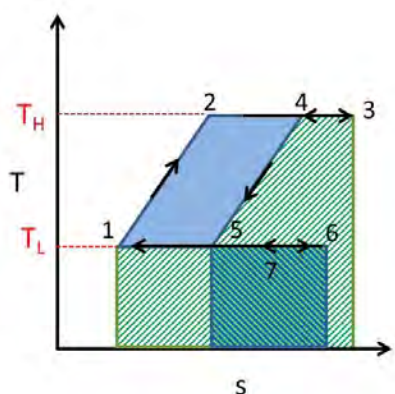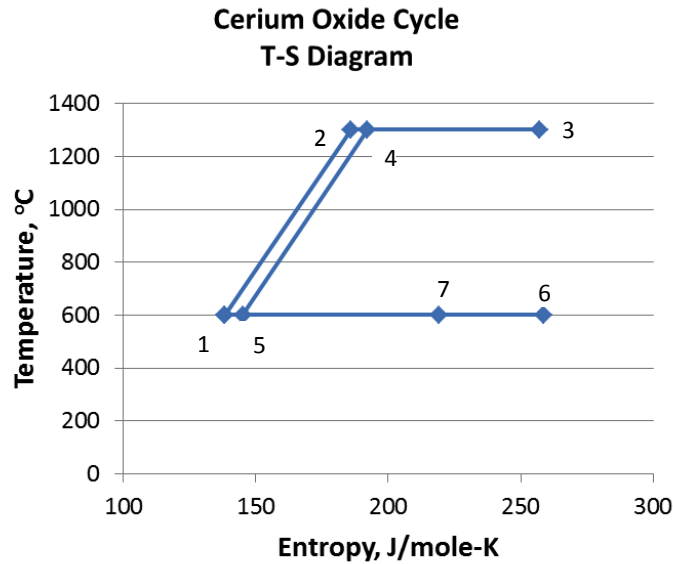

Figure 2-5. Generalized temperature-entropy diagram for the idealized cerium oxide cycle. The numbers illustrate state points in the analysis.

Utilizing published numbers for thermodynamic properties, the entropies, enthalpies, and enthalpy differences for the cycle steps can be calculated for $T_L = 600^{\circ}C$ and $T_H = 1300^{\circ}C$, Table 2-1, and plotted, Figure 2-6 [10].

Table 2-1. Thermodynamics of the Cerium Oxide Cycles for $CeO_2 \rightarrow \tfrac{1}{2}Ce_2O_3 + \tfrac{1}{2}O_2$ for $T_H = 1300^{\circ}C$ and $T_L = 600^{\circ}C$.

| State	Steps	T °C	S J/mole-K	H kJ/mole	ΔH kJ/mole
1	CeO_2 at T_L	600	138.337	-1048.967	
2	CeO_2 at T_H (reactor heat up)	1300	186.007	-992.03	56.937
3	$CeO_2 \rightarrow \tfrac{1}{2} Ce_2O_3 + \tfrac{1}{4} O_2$ at T_H (thermal reduction)	1300	257.0808	-800.4975	191.5325
4	$\tfrac{1}{2} Ce_2O_3$ at T_H ($\tfrac{1}{4} O_2$ sweep out)	1300	192.124	-811.3205	-10.823
5	$\tfrac{1}{2} Ce_2O_3$ at T_L (reactor cool down)	600	145.1665	-867.6005	-56.28
6	$\tfrac{1}{2} Ce_2O_3 + \tfrac{1}{2} H_2O$ at T_L (introduce water)	600	258.8115	-978.0655	-110.465
7	$\tfrac{1}{2} Ce_2O_3 + \tfrac{1}{2} H_2O \rightarrow CeO_2 + \tfrac{1}{2} H_2$ (re-oxidation)	600	219.289	-1040.584	-62.5185
1	CeO_2 at T_L (H_2 sweep out)	600	138.337	-1048.967	-8.383
				Σ ΔH	0

Figure 2-6. Temperature-entropy diagram for the idealized cerium oxide cycle using published thermodynamic values in which the reduction and oxidation reactions go to completion.

In reality, CeO_2 will not completely reduce to $\frac{1}{2}Ce_2O_3$ and re-oxidize back at 1300°C. Only a fraction of the $\frac{1}{4}$ moles of oxygen will be produced per cycle per mole of CeO_2. Partial reduction of CeO_2 can be expressed as $CeO_2 \rightarrow CeO_{2-\delta} + \frac{1}{2}\delta O_2$, where δ is the change in oxygen stoichiometry as mentioned before. In addition, with a packed bed reactor the reactor container must be heated and cooled each cycle, therefore, requiring additional heat to be added (state 1-2) and removed (state 4-5) each cycle. Assuming $\delta = 0.03$ and a containment heat capacity equivalent to 20% of the CeO_2 heat capacity, results in the state point thermodynamics in Table 2-2 and the T-s diagram in Figure 2-7.

Table 2-2. Thermodynamics of the Cerium Oxide Cycles for $CeO_2 \rightarrow CeO_{1.97} + 0.015O_2$ for T_H = 1300°C and T_L = 600°C. An additional 0.2 moles of non-reactive CeO_2 is assumed.

State	Steps	T ^{o}C	S J/mole-K	H kJ/mole	ΔH kJ/mole
1	CeO_2 at T_L	600	138.3370	-1048.9670	
2	CeO_2 at T_H (reactor heat up)	1300	186.0070	-992.0300	68.3244
3	$CeO_2 \rightarrow \frac{1}{2} Ce_2O_3 + \frac{1}{4} O_2$ at T_H (thermal reduction)	1300	190.2714	-980.5381	11.4920
4	$\frac{1}{2} Ce_2O_3$ at T_H ($\frac{1}{4} O_2$ sweep out)	1300	186.3740	-981.1874	-0.6494
5	$\frac{1}{2} Ce_2O_3$ at T_L (reactor cool down)	600	138.7468	-1038.0850	-68.2850
6	$\frac{1}{2} Ce_2O_3 + \frac{1}{2} H_2O$ at T_L (introduce water)	600	145.5655	-1044.7129	-6.6279
7	$\frac{1}{2} Ce_2O_3 + \frac{1}{2} H_2O \rightarrow CeO_2 + \frac{1}{2} H_2$ (re-oxidation)	600	143.1941	-1048.4640	-3.7511
1	CeO_2 at T_L (H_2 sweep out)	600	138.3370	-1048.9670	-0.5030
					0.0000

9
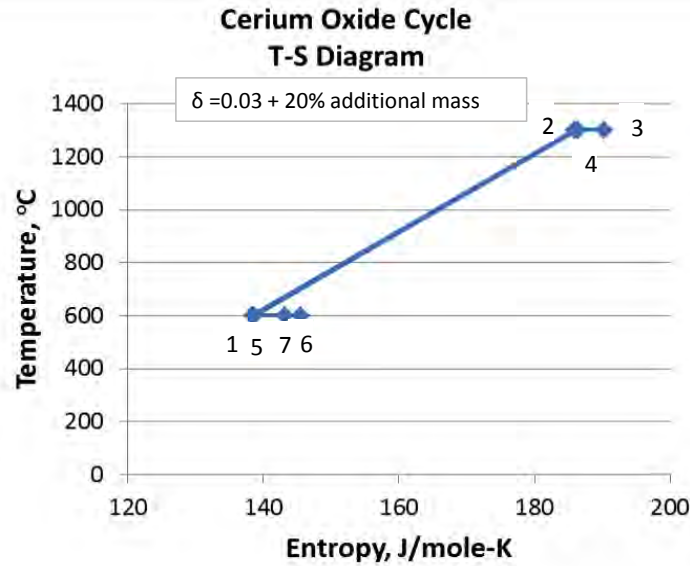
Figure 2-7. **Temperature-entropy diagram for the cerium oxide cycle assuming $CeO_2 \rightarrow CeO_{1.97} + 0.015O_2$ for $T_H = 1300^oC$ and $T_L = 600^oC$. An additional 0.2 moles of non-reactive CeO_2 is assumed to account for the mass of the reactor containment.**

Not accounted for in the above analysis is the amount of energy needed to vaporize and preheat the water to T_L. An evaluation of the waste heat available indicates that there is more than sufficient waste heat available to preheat the needed water. Table 2-3 shows the heat flows needed for preheating, vaporizing, and superheating the feed water along with the sensible heat available from cooling the product hydrogen and oxygen to ambient temperature for the idealized cycle (complete reduction/oxidation). Combined with the heat available from cooling the reduced ceria from T_H to T_L (state 4-5) and the exothermic heat of the oxidation reaction (state 6-7) there is more than ample waste heat (See Table 2-1). For the case illustrated in Table 2-2 and Figure 2-7, for example, in which ½ x 2δ moles of H_2 are produced, the preheat requirements to provide the stoichiometric required amount of water is only 0.03 x (2.833 + 20.436 + 9.181) = 0.9735 kJ, but there are 68.2850 + 3.7511 = 72.0361 kJ of waste heat available from the ceria alone. There is, therefore, sufficient waste heat to provide a large amount of excess water to the oxidation reaction.

Table 2-3. Water cycle analysis for $T_H = 1300^oC$ and $T_L = 600^oC$ for the idealized cerium oxide cycle.

| Water Cycle	T ^oC	S J/mole-K	H kJ/mole	ΔH kJ/mole	Comments
a. ½H$_2$O(l) at 25°C	25	34.975	-142.915		
b. ½H$_2$O(l) at 100°C	100	43.4485	-140.082	2.833	Sensible heating
c. ½H$_2$O(l) → ½H$_2$O(g) at 100°C	100	98.206	-119.646	20.436	H$_2$O vaporization
d. ½H$_2$O(g) at 600°C (superheat)	600	113.645	-110.465	9.181	Steam Superheat
e. ½H$_2$(g) at 600°C	600	80.952	8.383		
e'. 1/4 O$_2$(g) at T$_H$	1300	64.957	10.823		
f. ½H$_2$(g) at 25°C (cool down H$_2$)	25	65.3395	0	-8.383	Sensible heat in H$_2$
f'. 1/4 O$_2$(g) at 25°C (cool down O$_2$)	25	102.575	0	-10.823	Sensible heat in O$_2$

From the state point analysis it is possible to calculate a cycle thermal efficiency, η_{th}.

$$\eta_{th} = \delta \times \Delta H_{H2Ol} / Q_{in}$$

where $Q_{in} = Q_{sensible} + Q_{reaction}$. ΔH_{H2Ol} is the enthalpy of formation of liquid water, 285.83 kJ/mole, $Q_{sensible}$ is the heat needed to heat the cerium oxide to T_H (state 1-2), and $Q_{reaction}$ is the endothermic heat into the reduction reaction (state 2-3). If somehow the heat from cooling the reduced cerium oxide from

T_H to T_L (state 4-5) can be used to provide some $Q_{sensible}$, i.e., recuperation, input thermal energy requirements can be significantly reduced. Figure 2-8 shows the thermal efficiency of the cerium oxide cycle operating between $T_L= 600^{o}C$ and $T_H = 1300^{o}C$ and with a 20% effective containment mass as functions of oxygen stoichiometry change and recuperation efficiency, η_{rec}. Recuperation efficiency is a percent of the sensible heat from the reduced ceria (state 4-5) used for preheat (state 2-3).
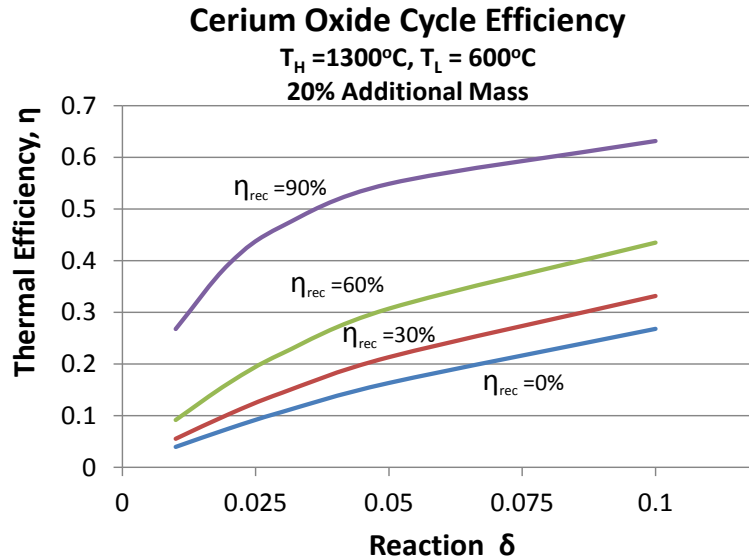
Figure 2-8. Thermal efficiency of the cerium oxide cycle as functions of oxygen reaction stoichiometry and recuperation efficiency operating at $T_H = 1300^{o}C$ and $T_L = 600^{o}C$, assuming an additional 20% effective containment mass.

2-2. Heat Pipe Based Reactor

A new heat pipe based solar reactor was designed and developed in this program. The focus was to increase the heat transfer area to enable rapid heating of the ceria-based material subject to a concentrated solar heat flux. In this design, the incident solar flux is directed into a cavity receiver containing one or more high-temperature heat pipes. Specifically, the evaporator of the heat pipe is connected to the cavity housing where the incident solar flux is then transferred to the heat pipe. The condenser end of the heat pipe is located outside of the cavity. The length of the condenser can be tailored to effectively spread the concentrated solar radiation over a large surface area. The porous ceria material is located around the condenser end of the heat pipe. *A key attribute of this design is that it enables the ceria material to be distributed over a large surface area (determined by the length and number of heat pipes) and provides a high degree of flexibility to optimize the heat transfer from the concentrated solar power to the ceria material*. Another advantage of a heat pipe based reactor is its ability to perform thermal cycling without moving parts. A combination of pressure controlled heat pipe (PCHP) and constant conductance heat pipe developed by ACT [11] enables the thermal load to be varied by adjusting the amount of the non-condensable gas at the condenser end of the heat pipe (Figure 2-9). In effect, controlling the amount of non-condensable gas controls the available heat transfer area at the condenser, which in turn enables the regulation of the CSP to the ceria material.
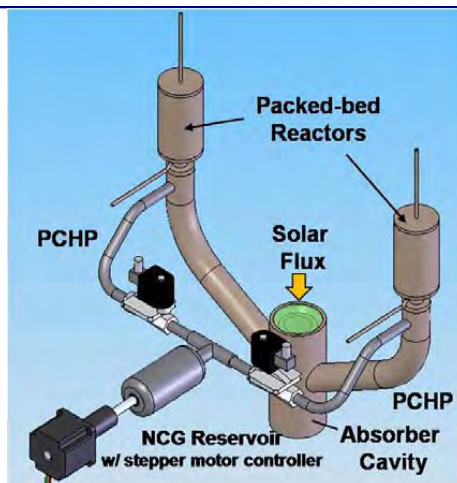
Figure 2-9. Schematic drawing of the heat pipe based reactor. Two reactors are cyclically heated by the solar energy. Pressure controlled heat pipes (PCHP), controlled by the amount of non-condensable gas (NGC), are used to perform the thermal cycle between two constant conductance heat pipe (CCHP) reactors.

The heat pipe can be thought of as a *thermal transformer* that converts the high heat flux solar energy from the solar receiver to a lower heat flux that is applied to heat the ceria material. In addition, the heat pipe reactor enables the material to be distributed over a large surface area (having a large surface area to volume ratio), which accelerates the transient thermal response of the material, shortens the reduction half-cycle time, and increases the system efficiency. Also, since the heat pipe reactor decouples the heat transfer area of the material (condenser area of the heat pipe) from heat transfer area of the cavity receiver (evaporator area of heat pipe), the solar receiver can be relatively small such that the overall heat loss (e.g., re-radiation through the aperture) can be minimized.

As mentioned earlier, the thermochemical cycle can be thought of in an analogous way to a thermodynamic cycle, in which mechanical work results from the net difference between the thermal energy into and out from the working fluid. In the thermochemical cycle, the chemical energy (enthalpy of combustion of H_2 or CO) obtained is equal to the net thermal energy difference applied to the ''working material'' (ceria). Dish Stirling engines provide a good example to further demonstrate how important heat transfer is in such systems. If the working fluid is helium, which has the second highest thermal conductivity among the gases (behind hydrogen), the cavity receiver can handle a heat flux capability ($\approx$ 75 W/cm^2) at elevated helium pressures. If the working fluid is changed to air, which has a much lower thermal conductivity, the power will be only 20 ~ 25% for the same displacement engine design [12], which is 4 ~ 5 times lower efficiency for the same input thermal power. For the thermochemical cycle, since the thermal conductivity of the working material is for the most part fixed, increasing heat transfer area is necessary to match the high heat flux inside the receiver with that which can be taken up by the material in an effort to approach the theoretical efficiency.

In spite of several advantages of heat pipe based reactor, the maximum temperature operation temperature is restricted by the envelope material and the working fluid. Heat pipes fabricated using superalloys have a temperature limit up to 1100°C. These were used in the Phase I study. In Phase II, however, refractory metals were needed to enable operation at higher temperatures ~1300°C. Details are described below.

3. Material Study

Though there are several attractive features of the two-step ceria based thermochemical cycle, the main challenge is the need for high temperature for the reduction step. CIT's previous studies demonstrated that Zr-substituted ceria (ZSC), specifically $Ce_{0.8}Zr_{0.2}O_{2-\delta}$ (ZSC20), has attractive characteristics for thermochemical water dissociation at reduced (*i.e.*, ≤ 1400°C) temperatures [13]. The properties of this material suggested, however, that a composition with lower Zr content might provide an even better combination of properties than either neat ceria, which needs very high temperature to achieve high efficiency, and ZSC20, which achieves high efficiency only when the temperature swing between T_H and T_L is wide and accordingly T_L is so low that kinetic limitations can be anticipated. Accordingly, the thermodynamic characteristics of low-Zr content (< 20%) ZSC compounds have been evaluated and their potential for water and CO_2 dissociation. Thermogravimetric measurements have been utilized to determine the thermodynamics of the oxidation/reduction reaction of ZSCs with a series of Zr-content (5%, 10% and 15%). Enthalpy and entropy for these compositions are both lower than that of neat ceria. Although the experimental data show that the correlation between thermodynamic properties and Zr content is not as simple as initially assumed (i.e. linear), efficiency analyses based on the thermodynamic properties supports the same conclusion as reported previously. Specifically, it remains the case that ZSCs are suitable for thermochemical dissociation of water and carbon dioxide at a reduced temperature (< 1500°C) at a better efficiency than neat ceria.

In addition to Zr-substituted ceria (ZSC), Praseodymium Cerium Oxide (PCO) materials have been identified as a potential class of materials for thermochemical hydrogen generation due to the potential application of the Pr^{III}/Pr^{IV} redox couple in the reduction and oxidation steps to generate hydrogen in tandem with the Ce^{III}/Ce^{IV} redox couple. In addition, due to the lower stability of the Pr^{IV} state compared to the Ce^{IV} state, Pr-substitution is anticipated to enable hydrogen production at lower temperatures than that required for neat CeO_2. The studies of both ZSC and PCO are described below.

3-1. Zirconium Doped Ceria

The composition 20% Zr (ZSC20) was initially selected as a model system and starting point for a comprehensive investigation of the role of Zr substitution on thermochemical cycling characteristics for fuel production. Thermodynamic calculations based on a simple linear interpolation of the thermodynamic properties with respect to Zr substitution level between neat ceria and ZSC20 indicated that lower (i.e. < 20%) Zr content materials may deliver superior fuel production characteristics than either of the end-member materials (CeO_2 and ZSC20). Accordingly, the properties of low Zr-content ZDCs have been the focus of this study. Specifically, the oxidation enthalpy and entropy, are determined by thermogravimetric analysis of samples with Zr = 5, 10 and 15 mol%. Using the measured values, efficiencies for thermochemical cycles are computed based on ZSCs at different Zr substitution levels and compared to those of neat ceria. In our previous analysis, the thermodynamic properties were taken to vary linearly as a function of Zr content in order to estimate efficiencies, and, thus, the present study reflects a significant experimental advance.

Sample Preparation
Oxide powders containing 5, 10 and 15 mol% Zr were prepared by a chemical solution process using nitrate sources. The resulting powders were confirmed to be single phase fluorite by X-ray powder diffraction, and the Zr substitution level was confirmed to be accurate by energy dispersive spectroscopy. From these, highly porous (> 80%) monoliths 500 ~ 700 mg in mass were prepared using a combination of mild compaction and light sintering (2 hr, 1500°C). The samples were placed atop a platinum foil to prevent any reaction between them and the alumina container during sintering.

Thermodynamic Properties

The thermodynamic properties of different ZSC materials were determined from a measurement of their weight under an atmosphere of controlled oxygen partial pressure (pO_2) over a wide range of conditions and temperatures up to 1490°C (Netzsch STA 409). Target oxygen partial pressured were achieved (a very low pO_2) by mixing H_2, H_2O and Ar in the appropriate ratios. At higher pO_2, simple mixtures of O_2 and Ar were used. The actual pO_2 was recorded using an oxygen sensor placed in close proximity to the sample at a downstream position. The large sample mass ensured good sensitivity. The results, Figure 3-1, show the nonstoichiometry, δ (deficiency in oxygen relative to the ideal formula, *i.e.* $Ce_{1-x}Zr_xO_{2-\delta}$), to increase monotonically and smoothly with increasing temperature and decreasing pO_2. In addition, for any given T and pO_2, the nonstoichiometry increases with increasing x.
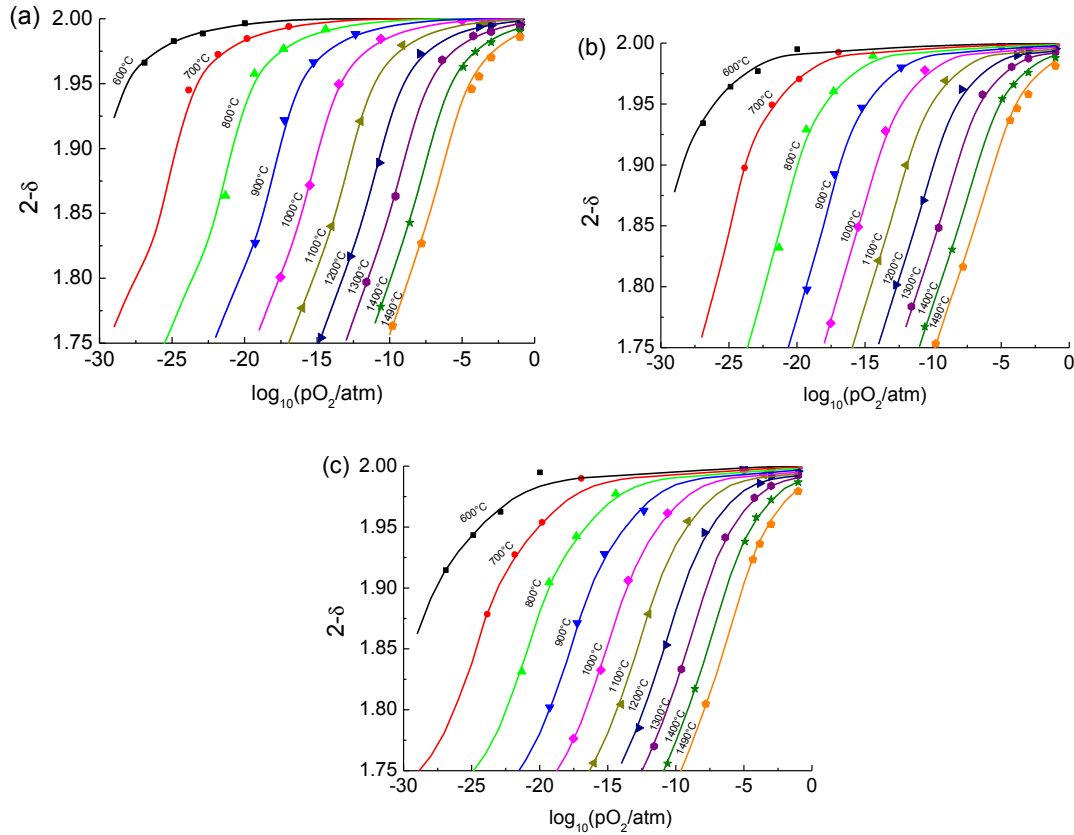
Figure 3-1. Nonstoichiometry of $Ce_{1-x}Zr_xO_{2-\delta}$ for (a) x = 0.05, (b) x = 0.10, (c) and x = 0.15 in the 600 - 1490°C range. Symbols are measurements and lines are calculated using the extracted thermodynamic properties (Figure 3-2).
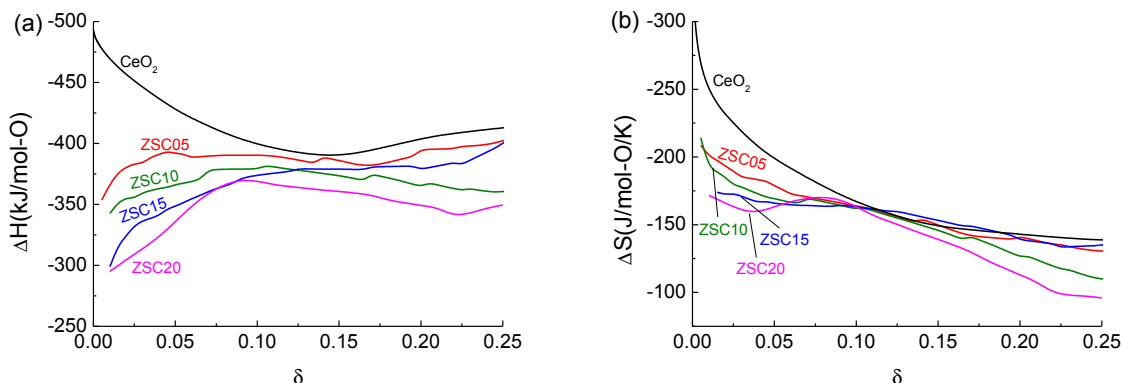
The thermodynamic properties of interest are the enthalpy (ΔH) and entropy (ΔS) of the ZSC oxidation reaction:

$$\lim_{\alpha \to 0} Ce_{1-x}Zr_xO_{2-\delta-\alpha} + \frac{\alpha}{2}O_2 \to Ce_{1-x}Zr_xO_{2-\delta}$$
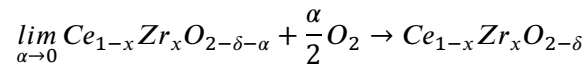
They are determined by evaluating the iso-stoichiometry curves relating pO_2 at given δ to temperature. Each set of iso-stoichiometry conditions yields a linear curve on an Arrhenius plot of $\ln(pO_2)$ vs $1/T$ (not shown). Assuming temperature independent properties (*i.e.*, the curves are linear), the slopes correspond to $\Delta H(\delta)$ and the intercepts to $\Delta S(\delta)$. The results are summarized in Figure 3-2, in which a comparison to the properties of neat ceria [13] and our earlier measurements of ZSC20 are also presented. To validate

14

the quality of the thermodynamic analysis and the accuracy of the derived properties, the nonstoichiometry was calculated using the ΔH and ΔS. The agreement between the calculated (solid curves in Figure 3-1) and measured values is satisfactory. Slight discrepancies, particularly at intermediate values of pO_2 (particularly evident for ZSC15) are likely due to gas leakage into the TGA and will be resolved in subsequent measurements. These discrepancies do not impact the overall conclusions.

The results of in Figure 3-2 show that, in general, the magnitude of ΔH and ΔS decrease monotonically with increasing Zr content. This reflects the overall increase in δ with increasing x at any given set of atmospheric conditions. This compositional trend in ΔH and ΔS is particularly clear for the $\delta < 0.10$ region, which is of the highest relevance for establishing efficiency under the operating conditions (T and pO_2) of interest to this study. The overall trends with δ are somewhat unfortunate. In contrast to neat ceria, all of the Zr substituted compositions show a significant decrease in the magnitudes of ΔH and ΔS at low δ. This is turns out to be precisely the opposite of what is desirable for a thermochemical oxide. In order to return δ to zero at low temperature, ΔH and ΔS should have large magnitude at low δ, whereas to release a large quantity of oxygen at high temperature, ΔH and ΔS should have small magnitude at low δ. However, the fact that the overall ΔG has decreased in magnitude does allow for thermochemical cycling at reduced temperatures relative to neat ceria, as discussed in terms of the efficiency calculations presented below.

Figure 3-2. Thermodynamic properties of the oxidation of $Ce_{1-x}Zr_xO_{2-\delta}$ (x = 0, 0.05, 0.10, 0.15, 0.20): (a) enthalpy of oxidation; and (b) entropy of oxidation. The data for ZSC20 are from our previous report, those for neat ceria are taken from reference [13].

Efficiency Analysis for Water and CO₂ Dissociation
Following an approach we have utilized previously [14], we note that the thermodynamic efficiency of the thermochemical approach for converting solar radiation and water to fuel can be written as:

$$h_{\text{solar-fuel}} = \frac{Q_{\text{fuel}}}{Q_{\text{solar}}}$$

where Q_{fuel} is the combustion heat of the fuel and Q_{solar} is the total heat input to the cycle (required to produce one mole of fuel). For the dissociation of water, we define Q_{fuel} as the higher heating value of one mole of hydrogen, and we take Q_{solar} to consist of re-radiation losses and three enthalpy terms: that required to heat water from 298 K to T_L, that to heat the ceria-based oxide (generically, $MO_{2-\delta}$) from T_L to T_H, and that to reduce the oxide from $MO_{2-\delta f}$ to $MO_{2-\delta i}$ at T_H. Together, these imply:

15

$$Q_{solar} = \frac{1}{\eta_{abs}}\left[n_{H_2O,i}\left(\Delta H_{H_2O(l)\to(g)}^{298K\to373K} + \int_{373K}^{T_L} C_{p,H_2O(g)}dT \right) + \frac{1}{\Delta\delta}\int_{T_L}^{T_H} C_{p,CeO_2}dT + H_{red}(T_H) \right]$$

where n_{H2O} is the moles of water heated per mole of hydrogen produced and $C_{p,j}$ is the molar heat capacity of species j at constant pressure. For the dissociation of carbon dioxide, due to the absence of phase change, Q_{fuel} is simply the combustion heat of CO, and Q_{solar} is:

$$Q_{solar} = \frac{1}{\eta_{abs}}\left[n_{CO_2,i}\int_{298K}^{T_L} C_{p,CO_2}\,dT + \frac{1}{\Delta\delta}\int_{T_L}^{T_H} C_{p,CeO_2}dT + \Delta H_{red}(T_H) \right]$$

For both cases, the absorption efficiency, η_{abs}, is calculated by assuming a blackbody receiver with an incident radiation flux of 5 MW m^{-2}. The change in oxide nonstoichiometry, $\Delta\delta$, which directly yields the quantity of fuel (hydrogen) produced, is taken from closed-system equilibrium calculations [14] using values of the input process parameter, $r_k = n_{i,k} / d_i n_{Ce_{1-x}Zr_xO_{2-d_i}}$ (k = H$_2$O or CO$_2$; "i" stands for "initial"),

the molar quantity of steam (or carbon dioxide) injected into the system at the initiation of the fuel production half-cycle relative to the available nonstoichiometry, that yield maximum efficiency. This ratio varies with cycling conditions and material composition and hence an iterative optimization is employed. The energy penalty associated with attaining the low oxygen partial pressure required in the reduction half-cycle (fixed here at 10^{-5} atm) is ignored in this analysis, including that of heating any sweep gases. These penalties can be expected to be specific to the reactor rather than the material. Finally, as this is purely a thermodynamic analysis, the impact of potentially slow kinetics is not captured.

The revised efficiencies, Figure 3-3, computed on the basis of the experimentally-derived ΔH and ΔS, show that, in agreement with the earlier calculations based on estimated ΔH and ΔS, the ZSC materials demonstrate a higher efficiency than neat ceria for reduced temperature cycling, that is, when T_H is 1300°C. Because the earlier result was based on interpolated thermodynamic properties and ΔH and ΔS clearly do not vary precisely linearly with Zr content (Figure 3-2), it is not surprising that the two sets of results differ in their details. As with the interpolated computation, we find now that in order to obtain high efficiency without recourse to unacceptably low T_L (which would undoubtedly have a negative impact on reaction kinetics) the Zr content should be small. In the case of ZSC 05, the highest possible efficiency (for hydrogen production) for T_H = 1300°C is 5.4% and is attained with T_L = 300°C. In the case of ZSC10, the highest efficiency is 5.9%, attained when T_L = 500°C.

At T_L = 600°C, at which reaction rates can be anticipated to remain satisfactory, ZSC10 provides the highest efficiency for either H$_2$O or CO$_2$ dissociation amongst all the compositions examined. The values, 5.1 and 5.0%, are approximately 20% higher than what is predicted from neat ceria, ignoring possible differences in kinetic responses. Such efficiencies, being rather low, point to the challenge of developing a ceria based oxide that will be effective at much reduced temperatures relative to the attractive values at T_H = 1500 to 1600°C. Even an increase in T_H to 1400°C provides a significant efficiency enhancement over T_H = 1300°C, for all of the compositions examined.
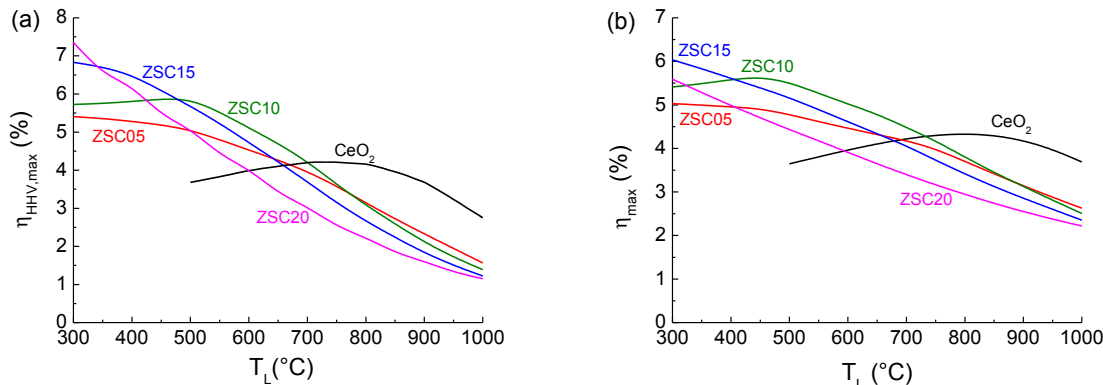
Figure 3-3. Calculated efficiencies of the zirconium substituted cerias studied as a function of T_L for fixed high temperature conditions of $T_H = 1300°C$ and $pO_2 = 10^{-5}$ atm: (a) for water dissociation, and (b) for carbon dioxide dissociation.

In terms of the influence of the reactant and product species, the efficiency of dissociating CO_2 is similar to that of dissociating water, with the former being slightly lower than the latter at $T_L < 800°C$, and vice versa at $T_L > 800°C$. This is because the equilibrium constant [15] (or equivalently the Gibbs free energy) of the $CO + ½O_2 = CO_2$ reaction is higher than that of $H_2 + ½O_2 = H_2O$ (i.e. CO_2 is more difficult to split than H_2O) below 800°C but higher than the latter above 800°C, as shown in Figure 3-4. At $T_L = 600°C$, efficiencies of 4.5% and 5.0% are computed from ZSC05 and ZSC10, respectively.
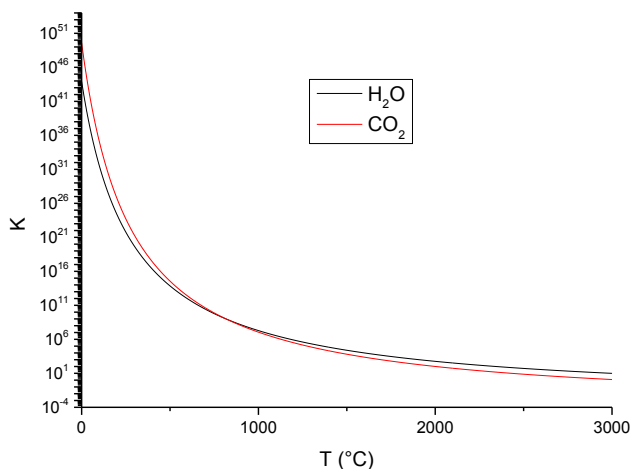
Figure 3-4. Equilibrium constants for the reactions $H_2 + ½O_2 = H_2O$ and $CO + ½O_2 = CO_2$ [15]. Note cross-over at ~ 800°C.

Summary and Outlook
High quality thermogravimetric data were collected to systematically investigate the variation with composition of the thermodynamic properties of Zr-substituted ceria materials underlying their thermochemical dissociation of water and CO_2. The experimental data confirm the previous conclusion that lightly Zr substituted compositions are more likely to deliver high efficiencies than those with high Zr content for cycles operating at reduced temperatures, e.g. $T_H = 1300°C$ and $T_L = 600°C$. The experimental data indicate that 10 mol% Zr is the optimum composition. Using this material and with $T_H = 1300°C$ an efficiency as high as 5.9% is predicted (for water dissociation), with a practical efficiency of 5.1% at $T_L = 600°C$. The energy efficiency for CO_2 dissociation is similar to that of water, with slight

17

differences due to the slight inherent thermodynamic differences between water and CO_2 thermal dissociation. These considerations alone would not drive a selection of one reactant gas over another.

3-2. Praseodymium Doped Ceria

Praseodymium Cerium Oxide (PCO) materials have been identified as a potential class of materials for thermochemical hydrogen generation. Here, the Pr^{III}/Pr^{IV} redox couple is used in the reduction and oxidation steps to generate hydrogen similar to the Ce^{III}/Ce^{IV} redox couple. In addition, due to the lower stability of the Pr^{IV} state compared to the Ce^{IV} state, Pr-substitution was then considered for hydrogen production as it enabled lower temperatures than that required for neat CeO_2. The following describes the preparation and characterization of PCO materials at various concentrations of Pr and their use for thermochemical fuel production.

Materials Preparation and Phase Behavior

Preparations of PCO materials used the solid-state reaction method, as reported by Chiba et al. [16]. It was discovered that these materials were chemically inhomogeneous (in contrast to the results of Chiba et al.) and our later studies have utilized chemical solution routes which readily yield homogeneous materials. In the case of solid state reaction, desired quantities of CeO_2 and Pr_6O_{11} were vigorously agitated with Y-stabilized ZrO_2 beads in an attritor mill for 6 hr, then calcined for 10 hr at 950°C. We attribute the lack of homogeneity to an insufficient milling time, but lengthening this step led to the presence of Zr impurities in the final material. In the case of chemical solution synthesis, a combined EDTA/citric acid sol-gel process was used with nitrate salts of Pr and Ce as precursors. The desired amounts of $Ce(NO_3)_3 \cdot 6H_2O$ and $Pr(NO_3)_3 \cdot 6H_2O$ were dissolved in water adjusted to pH 10 by ammonium hydroxide with 1.5 equivalents of EDTA and citric acid. Solvent was evaporated until gel formation was complete, after which the gel was fired overnight at $300 \sim 400$°C to form a black powder. The powder was then calcined at 950°C for 10 hr in air and annealed at 300°C for 10 hr, again, under stagnant air, to induce formation of the low temperature phase (200°C for 80PCO, 90PCO, and 95PCO).

The significant differences in the homogeneity of the resultant powders were evident from EDS (energy dispersive spectroscopy X-ray chemical analysis) measurements and from the breadth of the diffraction peaks observed in X-ray powder diffraction analysis of the materials, Table 3-1. For example, as prepared by solid state reaction, 60PCO (containing 60% Pr) exhibited Pr content ranging from 12% to 95% depending on the analysis site. In contrast, this sample composition prepared by chemical solution methods displayed a range of only 59.9% to 60.2%. Significantly, despite the wide variation in chemical composition, the majority of the solid state reaction prepared materials appeared by X-ray diffraction to be single phase (not shown). This is believed to be the result of the similarity in the ionic radii of Pr and Ce, such that oxides with differing Pr : Ce ratios display almost identical lattice parameters. Nevertheless, hints of the inhomogeneity of the materials can be observed in peak broadening in XRD diffractograms of materials prepared by solid-state reaction.

Table 3-1. Variation in Pr content by EDS and Peak Broadening in XRD

|	solid-state reaction preparations			sol-gel preparations	
	%Pr	FWHM (°)[a]		%Pr	FWHM (°)[a]
5PCO		0.20	5PCO	5.2(1)	0.14
10PCO	15(26)	0.17	10PCO	9.9(2)	0.14
20PCO		0.17	20PCO	20.1(1)	0.12
40PCO		0.17	40PCO	39.8(2)	0.14
60PCO	60(30)	0.20	60PCO	60.1(1)	0.13
80PCO	83(16)	0.24	80PCO	80.6(3)	0.10
			90PCO	90.6(5)	0.10
			95PCO	95.5(1)	0.11

[a]Full width at half max based on peak centered around 33° 2θ.

SEM micrographs of representative materials are shown in Figure 3-5. The XRD diffractograms for the $Ce_{1-x}Pr_xO_{2-\delta}$ materials prepared by chemical solution synthesis, Figure 3-6, show that a single cubic phase is observed at room temperature for Pr concentrations between 5 ~ 60%. The lattice constant of the cubic phase decreases very slightly with increasing Pr content over this range, from 5.411(1) to 5.401(1) Å, consistent with the slightly smaller Pr^{4+} ionic radius than that of Ce^{4+}, Table 3-2. At Pr concentrations of 80 and 90% two phases are observed: the cubic fluorite phase (CeO_2-type) and a phase with the Pr_6O_{11} structure type, a pseudo-cubic monoclinic phase [17]. At a 95% Pr, only the monoclinic phase is observed. The occurrence of the monoclinic phase, which presents strong reflections from a pseudo-cubic sublattice and weak reflections from the monoclinic superstructure, is evident from a close examination of the peaks in the vicinity of 42° 2θ, the position of the strongest of the weak superstructure peaks, (Figure 3-7). These weak reflections are clearly identifiable in 95PCO, are present though weaker in 90PCO, and are at the level of noise (or absent) in 80PCO. The cell volume of the pseudo-cubic monoclinic phase is larger than that of the fluorite phase (Table 3-2) consistent with the presence of a high concentration of Pr^{3+}, which has a substantially larger ionic radius than that of Ce^{4+} and Pr^{4+}. While the monoclinic superstructure peaks were not observed for 80PCO, the cell constant of the second phase is consistent with the interpretation presented. In addition, the slight increase in chemical inhomogeneity of the 80PCO and 90PCO compositions relative to the others (Table 3-1) and the slight decrease in peak breadth in the diffraction patterns from these materials, are also consistent with the presence of two phases.

It is of some note that the behavior observed here differs somewhat from what has been reported previously in the literature. Specifically, Chiba, et al. [16] have reported that the fluorite phase of CeO_2 can dissolve as much as 90% Pr. Only for the end-member Pr compound is the monoclinic phase observed. This discrepancy may be due to a difference in low temperature equilibration procedures, but this remains an open question. It is possible that further incorporation of oxygen into our 80PCO and 90PCO materials may transform them to single phase fluorite-type materials.
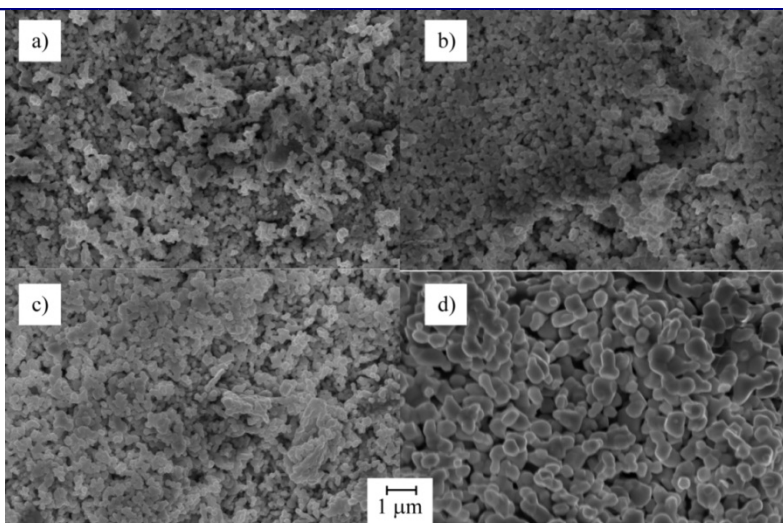
Figure 3-5. SEM micrographs of a) 20PCO, b) 40PCO, c) 60PCO, and d) 80PCO prepared by chemical solution routes.
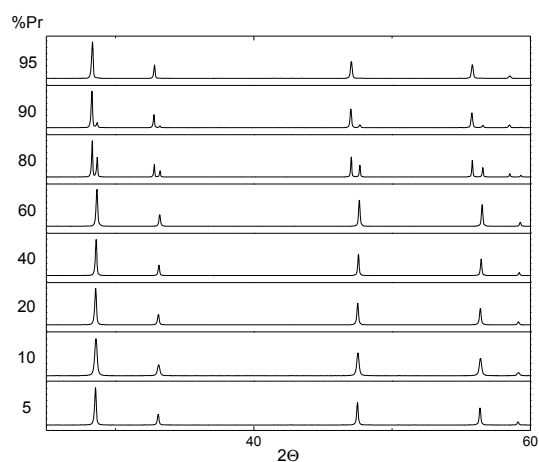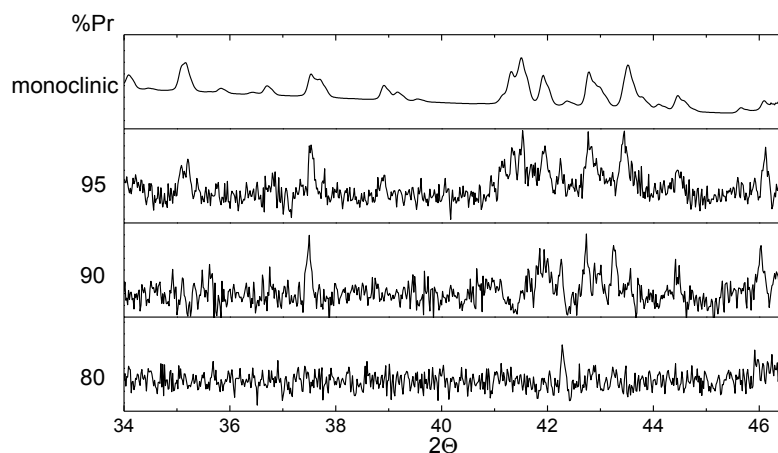

Figure 3-6. Powder diffractograms of PCO materials prepared by chemical solution routes with Pr content ranging from 5 ~ 95%.

Table 3-2. Lattice Constants for PCO materials[a]

| % Pr	cubic	psuedo-cubic	wt % pseudo-cubic
5	5.411(1)		
10	5.410(1)		
20	5.408(1)		
40	5.405(1)		
60	5.401(1)		
80	5.397(1)	5.465(1)	60.3(3)
90	5.395(1)	5.466(1)	89.8(3)
95		5.467(1)	100

[a]Determined by Rietveld refinement

20

%Pr

Figure 3-7. Powder diffractograms of 80PCO, 90PCO, 95PCO from 34 ~ 47° 2θ compared to the calculated diffractogram of monoclinic Pr₆O₁₁.
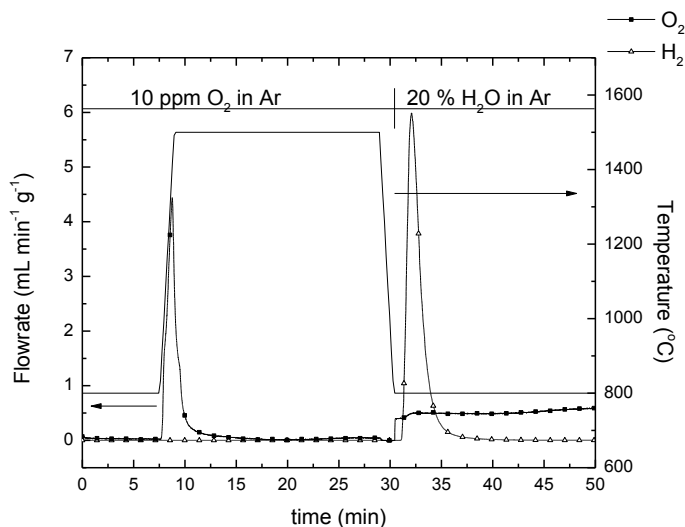
Thermochemical Cycling

Evaluation of high temperature behavior was carried out by in-situ X-ray diffraction (40PCO) and by measurement of fuel production (10PCO). For X-ray measurements, the solid state reaction produced material was measured under air at temperatures between 100 and 1200°C. The material was initially heated at 20°C min^{-1} to 800°C, then 10°C min^{-1} to 1200°C and held for about 4 hr. Diffractograms were obtained at 100°C increments on cooling at 10°C min^{-1} between 1200 and 800°C or 20°C min^{-1} between 800 and 100°C, with an equilibration of 20 min. at each temperature before collection. The material evidently transforms from a single cubic phase to a two-phase mixture at temperatures of 500°C and greater, (Figure 3-8). Because of the chemical inhomogeneity of this material, detailed analysis has not been performed. Nevertheless, the results suggest that the abrupt weight loss observed in the $Ce_{1-x}Pr_xO_{2-\delta}$ system under air for $0.9 < x < 0.4$ in the vicinity of 400 to 600°C may involve sharp changes in phase rather than merely loss of oxygen from a given structure with fixed crystalline arrangement. Remarkably, even if a phase change is involved, the results of Chiba et al. suggest a high degree of reversibility in the weight loss/gain behavior, in particular for the composition $Ce_{0.4}Pr_{0.6}O_{2-\delta}$. Almost no hysteresis in weight, as recorded on heating and cooling at 10°C/min under air, was reported, despite a weight loss corresponding to an extremely large $\Delta\delta$ of 0.11 at ~ 460 °C.

°C
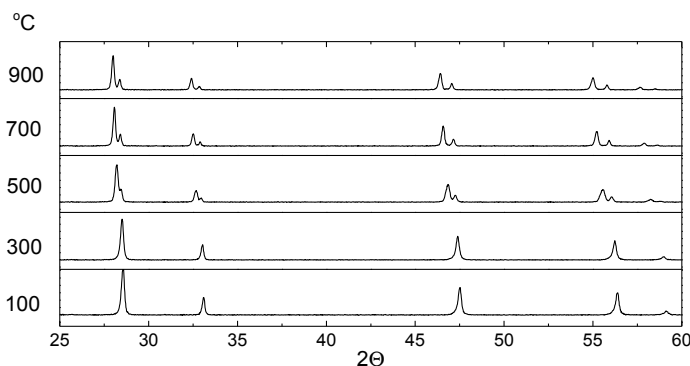
Figure 3-8. Powder diffractograms of SSR 40PCO from 100 – 900 °C.

The thermochemical cycling experiments were performed on porous pellets of the 10PCO material obtained from chemical solution synthesis. Porous pellets were prepared by pressing ~ 0.4 g of powder by hand wetted with isopropanol and fired at 1500°C for 6 hr, resulting in a pellet with 38% porosity.

Reduction was carried out under 10 ppm O_2 (balance Ar), at a flowrate of 1000 mL min^{-1} and a heating rate of 500 °C min^{-1}. The hold time at the high temperature was 10 min. The oxide was then quenched to the low temperature at a rate of 500°C min^{-1} and exposed to steam (20% H_2O, balance Ar) at a flowrate of 100 mL min^{-1} for a period of 25 min, at which point the gas was returned to 10 ppm O_2, held at temperature for 8 min, and the cycle repeated (Figure 3-9). The evolved gases were monitored by mass spectrometry, with a temporal rate of data acquisition of 140 cycles min^{-1}. The first set of cycling results, Figures 3-9 and 3-10, reveal Pr-doping to be indeed a promising approach. The PCO material shows reproducible oxygen release and hydrogen production over seven cycles, Figures 3-10 and 3-11, indicating stability under the reaction conditions. The amount of fuel produced per cycle, 9.3 ~ 9.8 mL H_2 per gram of oxide, is slightly higher than the expected value for undoped ceria subjected to similar cycling conditions (8.6 mL g^{-1}) based on the reported thermogravimetric data [13] and what we have measured previously [5]. At this stage it is unclear if higher fuel productivity for the Pr-doped material is due to truly higher activity. Potential errors with temperature calibration have to be ruled out. Another important result is the consistent observation of a 2 : 1 ratio of H_2 production to O_2 release (Figure 3-11). This result indicates that every oxygen vacancy created at high temperature is accessible and used for fuel production at low temperature. Finally, the reaction rates are also quite attractive. The peak oxygen release rate of 4.4 ml min^{-1} g^{-1} is comparable to what we have observed with undoped ceria. The hydrogen release rate in PCO attains a peak value of ~ 5.8 mL min^{-1} g^{-1}, Figure 3-9, only slightly lower than the value of ~ 9.8 mL min^{-1} g^{-1} attained with undoped ceria, and the difference may be due to slight differences in experimental conditions (lower gas flow rates in the current experiments) rather than differences in material properties. Furthermore, the time scale for the reaction completion, on the order of 8 min, remains fast relative to the other processes in the thermochemical reactor. The ease with which the nonstoichiometry of PCO materials, particularly with higher Pr content, can be changed at low temperatures [16] suggests that even more attractive cycling properties will be obtained at reduced temperatures at which undoped ceria is no longer effective. Such experiments are the subject of current work.

Figure 3-9. Gas production of H$_2$ and O$_2$ for 10PCO in one cycle between 1500°C and 800°C with temperature profile and inlet gas composition. Integrated oxygen flow amounts to 5.0 mL g^{-1} and that of the hydrogen flow to 9.8 mL g^{-1}.
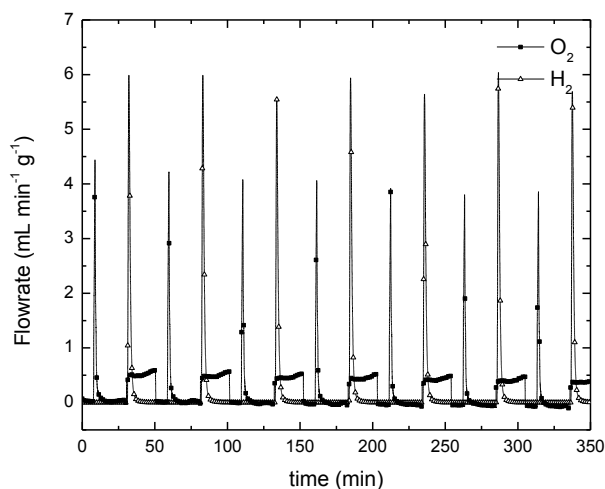
Figure 3-10. Thermochemical cycling of 10PCO between 1500°C and 800°C over 7 cycles. The sharp drop in oxygen signal towards the end of each low temperature step (not present in the data of Figure 3-9) is an artifact of changes in gas flow rates and is not a reflection of anomalous material behavior.
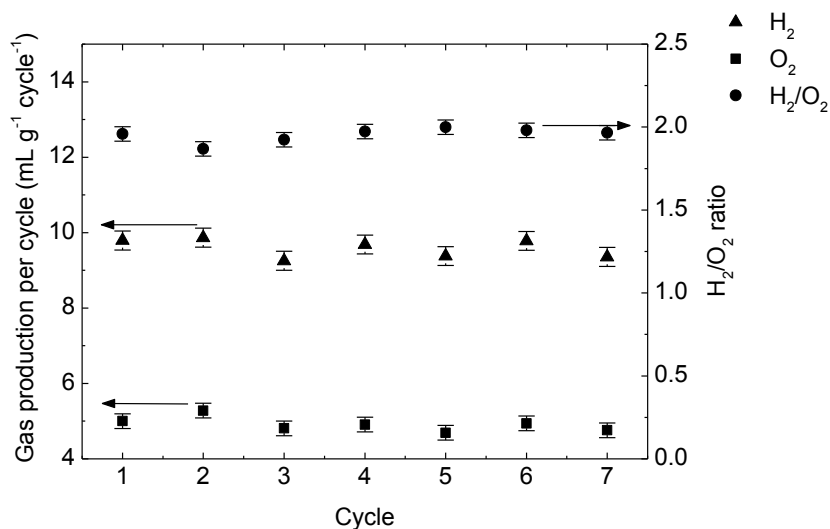
Figure 3-11. Gas production per cycle of H₂ and O₂ for 10PCO cycling between 1500°C and 800°C over 7 cycles with H₂ : O₂ ratio per cycle.

4. Heat Pipe Based Reactor Design

4-1. Superalloy Heat Pipe Based Reactor

To evaluate the feasibility of a heat pipe based reactor, a superalloy based heat pipe was first considered because it is capable to operate in an open atmosphere environment and materials are readily available. ACT also has a product line for superalloy heat pipe related products and extensive experience making these pipes. A single superalloy based heat pipe reactor system was designed and tested. An overall schematic of the system is shown in Figure 4-1. The packed bed reactor contains a porous sintered zirconia-ceria material. The material was synthesized from micron-size cerium oxide (CeO_2) and zirconium oxide (ZrO_2) powders that were ball milled and sintered at 1500^oC for 24 hours. The packed bed was formed in an annular configuration and positioned concentrically around a high-temperature heat pipe that both transferred heat into the reactor and aided in isothermalizing the packed bed. Haynes 230 was chosen as the heat pipe envelope based on its excellent creep strength, oxidation resistance, ability to machine, and ability to operate continuously at temperatures up to 1100^oC. The internal working fluid in the heat pipe was sodium, which is effective at temperatures up to 1100^oC.
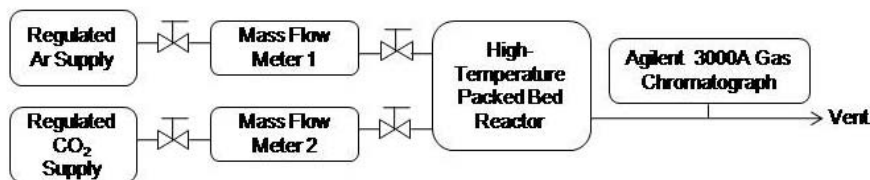

Figure 4-1. Overview of the experimental thermochemical reactor system.

An image of high-temperature reactor is shown in Figure 4-2A along with photos of the actual hardware (Figure 4-2B) and reactor housing (Figure 4-2C). At the base of the reactor, a SiC spiral heater element (I Squared R Element Co.) was positioned concentrically around the evaporator-end (bottom) of a vertically oriented constant conductance heat pipe (1" diameter and 12" long). The resistive heater element simulated the incident concentrated solar flux that can be generated from a solar collector. The heat was transferred upwards into the reactor volume, which contained the packed bed material (67 g) in the annulus (4.45 mm wide) between the outer wall of the heat pipe and the inner wall of the reactor housing; it was concentrically located around the condenser-end (top) of the heat pipe. The heat pipe also aided in isothermalizing the packed bed (Figure 4-3A). Figure 4-3B shows the initial testing of the heat pipe prior to integration with the reactor assembly.

24

(A)   **(B)**   **(C)**
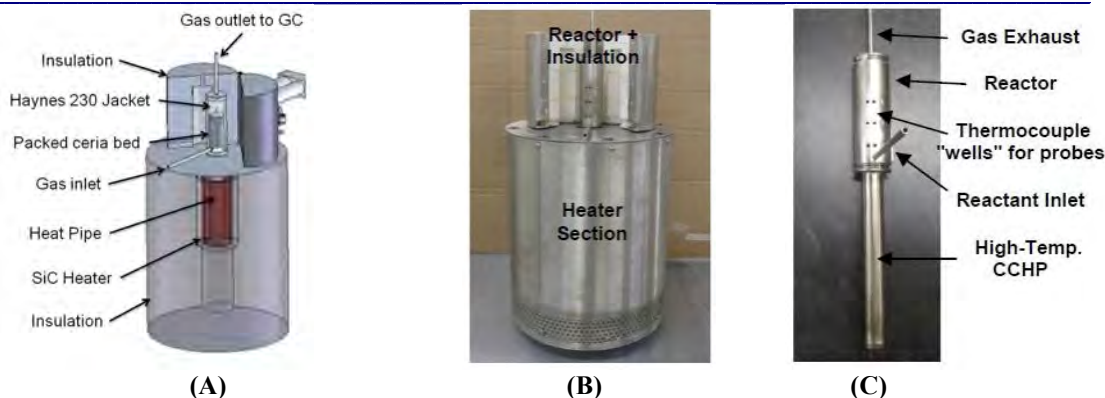
Figure 4-2. (A) Schematic of the experimental setup containing a silicon carbide heating element (heater can be heated to 1650°C; heat pipe can be used up to 1050-1100°C). (B) Actual test section, insulation and reactor housing. (C) Heat pipe and reactor.


(A)   **(B)**
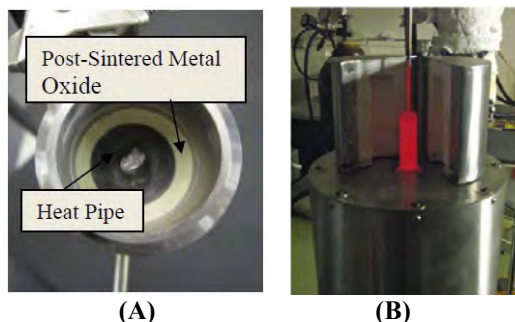
Figure 4-3. (A) The packed bed surrounds the heat pipe obtaining high heat transfer area. (B) Testing of the heat pipe at high-temperature (1050°C) showing relative isothermality (uniform red color) prior to integration with the reactor assembly.

The experimental reactor was thermally cycled and the axial and the radial temperature distributions in the packed bed were recorded. A PID controller was used to regulate the power to the SiC heater based on feedback from a thermocouple in contact with the base of the heat pipe (T_{base}). Three temperature measurements ($T_{1,inner}$, $T_{2,inner}$, $T_{3,inner}$) were taken at 3 different axial locations along the condenser section of the heat pipe (in the reactor section, coinciding with the I.D. of packed bed) and three measurements ($T_{1,outer}$, $T_{2,outer}$, $T_{3,outer}$) were taken at the outer radius of the packed bed at the same axial locations as the inner temperature measurements. All thermocouples were Omega Clad XL 0.0625" sheathed Type K. Here it should be noted that the thermocouples were inserted in "thermal wells" made from 0.25" O.D., 0.080" wall thickness Haynes 230 tubing that was welded closed at their interior ends and welded circumferentially to the outer reactor housing. These welds prevented air leaks from the reactor that could adversely affect the fuel productivity. Additionally, the temperature measurements across the packed bed ($T_{i,outer}$ - $T_{i,inner}$) provided information on the radial temperature gradient across the packed bed. This is important since the relatively low thermal conductivity of the porous metal oxide limits the rate at which heat transferred from the heat pipe propagates radially into the ceria material. In turn, the temperature nonuniformity in the reactor affects the overall extent that the material can be reduced during the thermal reduction half-cycle (i.e., nonstoichiometry of the material). A spatial variation in the nonstoichiometry of the material will then affect the amount of fuel produced within the reactor during the re-oxidation half-cycle, i.e., reduce the amount of fuel produced relative to that which could otherwise be produced if the material was uniformly reduced at the higher temperature (inner temperature of the metal oxide).

During the high-temperature thermal reduction half-cycle, a "low oxygen content" Argon sweep gas (Praxair, Research Grade 6.0, 99.9999% purity) continuously flowed through the reactor at a prescribed flow rate. Oxygen gas released from the metal oxide was swept downstream and measured using an Agilent 3000A micro-gas chromatograph (GC) equipped with PoraPlotU and MolSieve 5A columns. During the lower temperature re-oxidation half-cycle, the inert sweep gas was turned off and CO_2 and/or H_2O vapor were introduced into the reactor (in some cases, CO_2 and H_2O were premixed with the sweep gas) at a prescribed mass flow rate. The effluent from the reactor was analyzed approximately every 3 minutes with the GC and the composition (i.e., H_2, CO, CO_2, etc.) determined.

Thermal Behavior of the Heat Pipe Reactor

The inner and outer temperature measurements of three different locations of the reactor are shown in Figure 4-4A and B. The axial temperature difference along the reactor ($T_{3,\,inner} - T_{1,\,inner}$) was about 40°C for $\approx$ 5 cm distance. A representative plot of the average temperature difference across the packed bed is shown in Figure 4-4C based on the average of the temperature measurements taken at the three axial locations. As shown, the temperature difference across the packed bed asymptotes to $\approx$ 20°C at about ~1/3 of the thermal reduction half-cycle and about 10°C during the re-oxidation half-cycle.

(A)	(B)	(C)
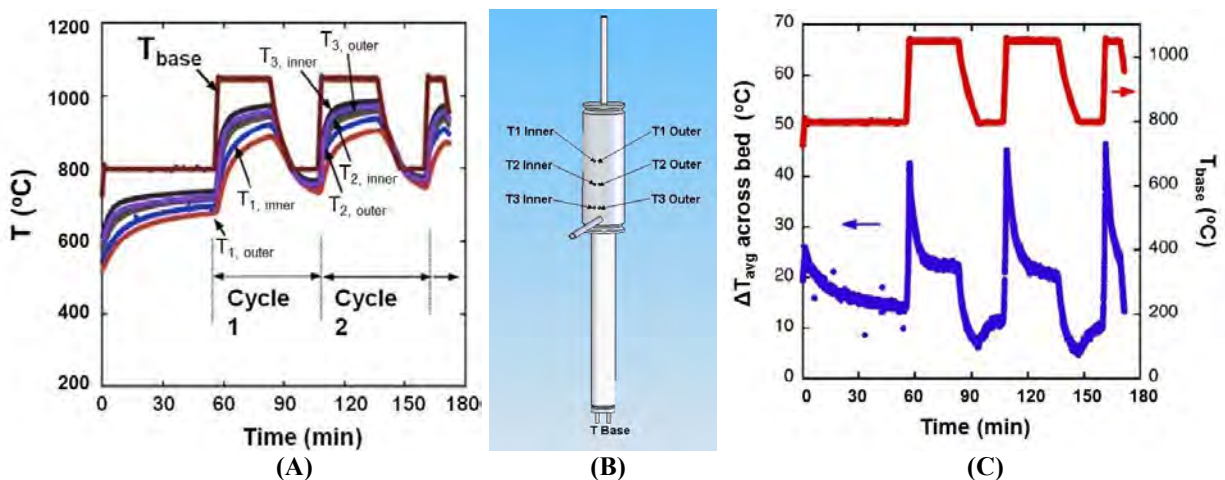
Figure 4-4. (A) Temperature histories associated with thermal cycling of the zirconia-ceria material in the reactor; 1 SLPM Ar sweep gas. (B) The axial locations of the thermocouples measured from the base of the reactor housing upwards were: 2.22 cm, 4.76 cm, and 7.30 cm for T3, T2, and T1, respectively. "Inner" refers to the temperatures measured in the thermal wells closest to the heat pipe wall and "outer" refers to the outer radii of the packed bed nearest the internal wall of the reactor housing. (C) Average temperature difference across the packed bed as the function of time (1 SLPM Ar flow).

O_2 *Evolution and* CO_2 *Dissociation*

The dissociation of water and carbon dioxide are similar; as such, for convenience, dissociation of CO_2 was considered here. Figure 4-5 shows the oxygen and CO evolution rates in the reactor. The O_2 and CO concentrations (percentages by volume) of the downstream products were determined by gas chromatography and their evolution rates were then computed knowing the Ar and CO_2 flow rates. While the overall fuel productivity was relatively low as compared with other reported results [3] (for which thermal reduction was at 1500°C as opposed to the 1000 ~ 1100°C temperatures used in this study), one interesting result was that the time for oxygen release was relatively short (80% of the O_2 produced in ~ 32 min). It is believed that the large heat transfer area contributed to the relatively small temperature gradient across the material (as shown in Figure 4-4C) and overall short time required for the oxygen release. Another note is that the CO generation rate was comparatively slow (80% of CO produced in ~47 min.), perhaps not unexpectedly because the doped zirconium slows the kinetics of the re-oxidation reaction.
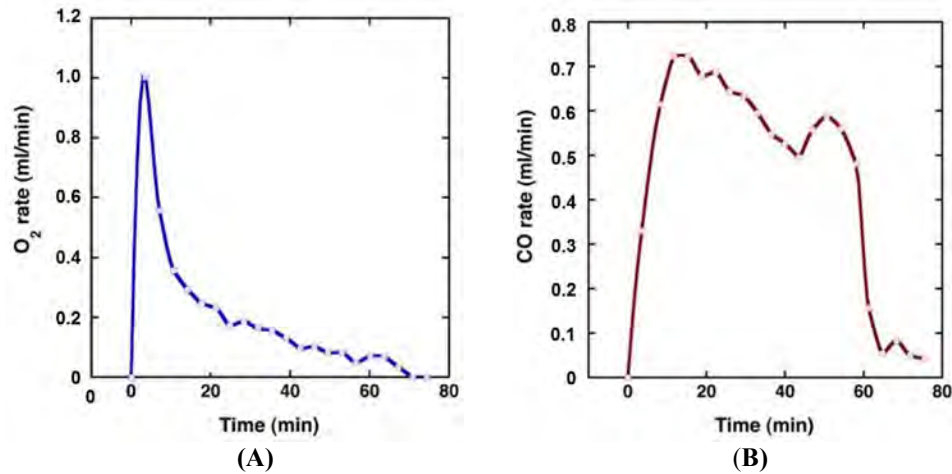
(A)   (B)

Figure 4-5. (A) O$_2$ evolution rate during thermal reduction reaction. Q$_{Ar}$ = 1 SLPM. (B) CO evolution rate during re-oxidation reaction. Q$_{CO2}$ = 4 SLPM.

4-2. Refractory Metal Heat Pipe Based Reactor

The maximum temperature limitation of Ni-superalloy heat pipes is 1050-1100°C due to the creep stress created by the elevated sodium vapor pressure at high temperature. According to the CIT's research on doped ceria, 1100°C is not sufficient to obtain a high fuel conversion efficiency using a two-step thermochemical cycle. Higher temperatures are needed for thermal reduction. This, a heat pipe that can handle higher temperatures was developed. Regarding the selection of the working fluid, a low vapor pressure working fluid, i.e., lithium, is used. Figure 4-6A shows the vapor pressure of different alkali metals [18]. At 1300°C, for example, sodium has a vapor pressure greater than 10 atm while lithium's is less than 1 atm at the same temperature. Lithium also has a high specific heat, low viscosity, and is the best heat pipe working fluid for the 1300°C range. In addition to its low vapor pressure, it has a high figure of merit at higher temperature, as shown in Figure 4-6B) that makes it an ideal working fluid for the desired temperature range. However, lithium is not compatible with nickel-based superalloys. Instead refractory metals are needed for the envelope material. Table 4-1 shows the compatibility and working temperature range of heat pipes with different structural materials and working fluids.
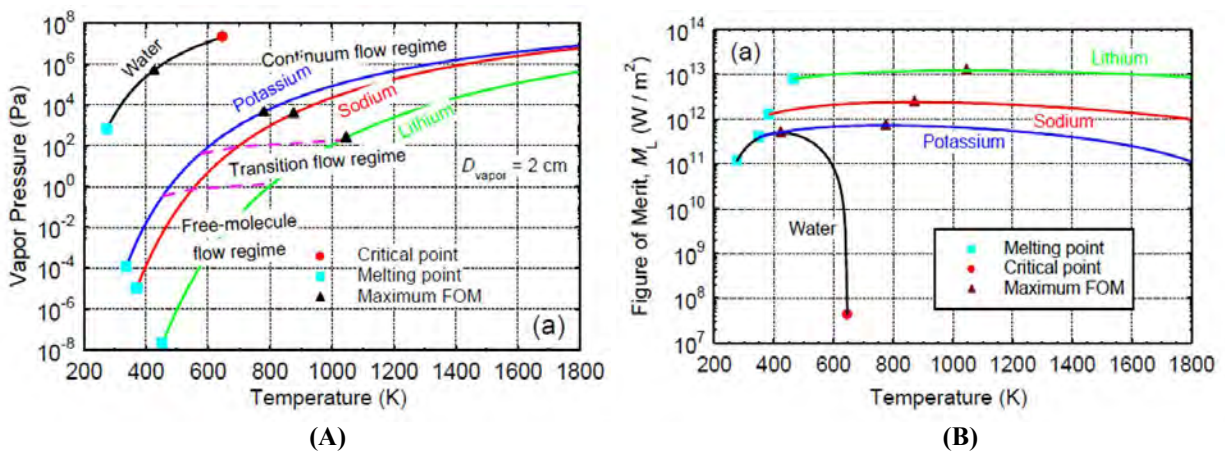

(A)   (B)
Figure 4-6. (A) Alkali metal vapor pressure. (B) Alkali metal figure of merit (FOM) [18].

Table 4-1. Compatibility and working temperature of alkali metal heat pipe [18].

Material	Temp. (K)	Compatibility	Material	Composition (Elements > 1%)	Melting (K)	Density (g/cm³)
Titanium	775 – 875	K	Titanium	Ti	1941	4.51
Steel alloys	875 – 900	Na, K, Hg	SS-304	Fe-19Cr-(8-12)Ni-2Mn	1699	7.92
			SS-316	Fe-17Cr-(10-14)Ni-2Mn	1658	7.9
Superalloys	900 – 1150	Na, K	Inconel 750X	73Ni-15.5Cr-7Fe-2.5Ti-1Nb	1666	8.25
		Na, K, NaK	Hastelloy X	49Ni-22Cr-15.8Fe-9Mo	1523	8.2
		Na	Haynes-25	50Co-20Cr-15W-10Ni-3Fe-1.5Mn	1602	-
Niobium alloys	Up to 1500	Li, Na, K	Niobium	Nb	2750	8.57
		Li, Na, K, NaK	Nb-1%Zr	Nb-1Zr	2680	8.58
			PWC-11	Nb-1Zr-0.1C	2680	8.60
			C-103	Nb-10Hf-1Ti-0.5Zr	2623	8.86
Molybdenum alloys	Up to 1800	Li, Na	Molybdenum	Mo (brittle below ~ 400 K)	2896	10.28
		Li, Na, K	Mo-TZM	Mo-0.5Ti-0.1Zr	2896	10.16
		Li	Mo-44.5%Re	Mo-44.5Re	3023	13.5
Tantalum alloys	Up to 2200	Li, Na, K, NaK, Hg, Cs	Tantalum	Ta	3290	16.6
			T-111	Ta-8W-2Hf	3250	16.7
			Astar 811C	Ta-8W-1Re-0.7Hf-0.025C	-	-
Tungsten alloys	Up to 2200	Li	Tungsten	W (brittle below ~ 600 K)	3695	19.25
			W-4%Re	W-4Re	-	18.35
Carbon	Up to 3000	Needs metal liner	Carbon	C	3923	2.25

Refractory metals have very high melting temperatures and include W, Mo, Ta, Nb, and Re, which have melting points above 2000°C. They are compatible with lithium and have very good creep resistance. Among different refractory metals and their alloys, TZM (molybdenum alloy with 0.5% titanium and 0.08% of zirconium and trace amount or carbon) is relatively easy to machine and has better mechanical properties compared to pure molybdenum due to the formation of carbides that prevent recrystallization at high temperature. It is also the most widely used molybdenum alloys. Compared to superalloys, refractory metals show much better mechanical properties at elevated temperature. Figure 4-7 shows the yield strength of Ni based superalloys and refractory metal molydenum alloys [19, 20]. As can be seen, TZM has much higher yield strength at temperature above 1100°C. Consequently, a lithium charged TZM heat pipe that has working temperature range up to 1500°C (Table 4-1) was chosen for the project.

(A)   (B)
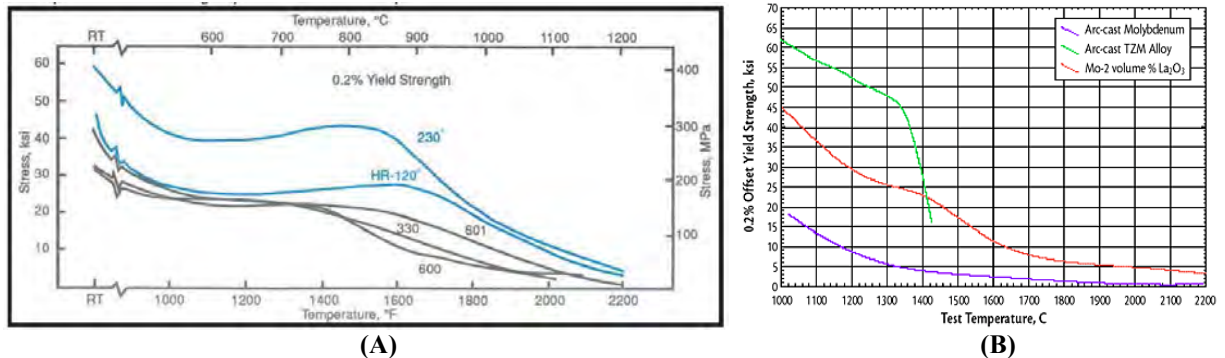
Figure 4-7. Yield strength at different temperature. (A) Superalloy [19]. (B) Moly alloy [20].

While refractory metals have superior mechanical properties at elevated temperature and are compatible with Li, a major issue with refractory metals is their poor oxidation resistance. Rapid oxidation occurs for moly alloys at temperature above 550°C and moly oxides have relative low melting points and therefore cannot form a protective passive layer as nickel oxide does. One way to prevent the oxidation is to coat a protection material. However, different coating materials have been explored yet most of the oxidation resistance coatings have insufficient life times (< 1000 hr as shown in Figure 4-8 [21]). An alternative option is to operate in an oxygen deficient environment, for example, vacuum or inert gas environment. Since radiation is the dominant heat transfer method at high temperature, one option is to operate the

TZM-Li heat pipe in a vacuum environment and radiatively heat the working material with the couple the heat pipe, which was the approach taken here.
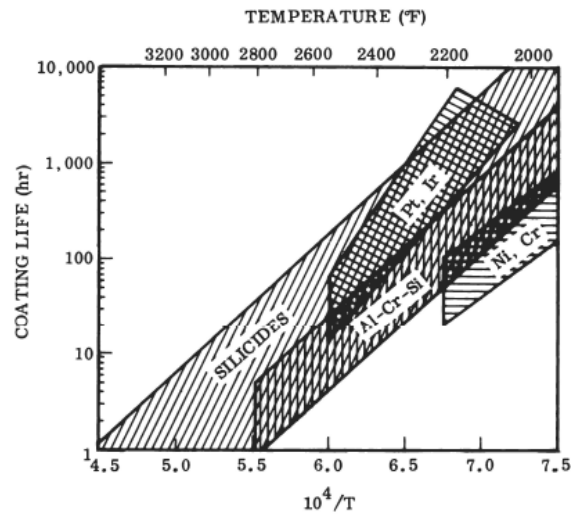

Figure 4-8. Performance capabilities of passivation coatings for molybdenum in air at atmospheric pressure [21].

Manufacturing of Refractory Metal - Lithium Heat Pipe

Manufacturing refractory metal heat pipes requires advanced machining and welding (e-beam) techniques, and procedures that are substantially than that used to make superalloy heat pipes. Moreover, they are very brittle at room temperature and extremely susceptible to oxidation at elevated temperatures. Thus, we operated them in a vacuum environment to avoid oxidation.

All heat pipes also have a fill tube for charging the working fluid; with refractory metals, conventional techniques to close/ pinch-off the tube and weld it sealed are not feasible (traditional sealed tube shown in Figure 4-9A). An alternative method used to seal the tube (developed by RCA in 1970s) involves passing a high current (~500+ Amps) through the tube in a vacuum chamber to melt/"burn-off" the tube and form a closed joint (Figure 4-9B). Specifically, tapered tubes are used such that the smallest area results in the highest electrical resistance and therefore the hottest spot location/ melt zone is controlled. In addition to the fill tube closing procedure, alkali metals, especially lithium, are very strong oxygen getters; as such, the oxygen has to be removed from the working fluid to avoid corrosion of the refractory metal envelope. Therefore, purification of lithium is required before it is charged in the refractory metal heat pipe.
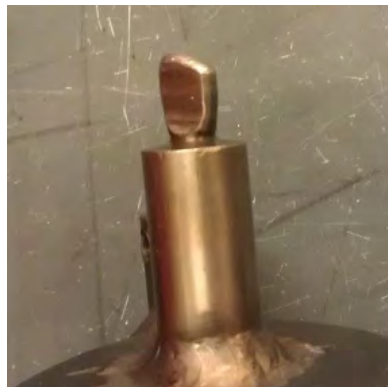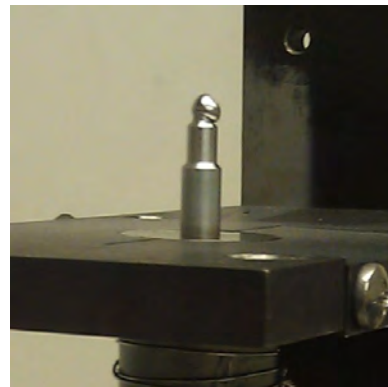
| (A) | (B) |

Figure 4-9. (A) Pinch off seal. (B) Burn off seal.

To minimize the oxygen content in the lithium, two purification procedures, cooking with oxygen getter material and low temperature filtration, were performed [22]. Lithium oxide is reduced by the metal based oxygen getter at high temperature (Gibbs free energy < 0). Yttrium chips was chosen for the oxygen getter. After cooking with the oxygen getter, the oxygen concentration was further lowered by passing the molten Li through a filter at a temperature just above its melting point. The solubility of oxygen decreases as temperature decreases and the non-dissolved lithium oxides were filtered out before the lithium was charged to the pipe. Figure 4-10A shows the lithium purification and charge setup.

After the lithium was charged, the heat pipe was moved to the bell jar vacuum chamber to perform a so-called "burp-off" procedure in which non-condensable gas is removed and the fill tube is "burn-off" to seal the tube. An induction heater was used to heat up the evaporator section of the pipe. As the temperature of evaporator increased, the lithium vapor pressure increased and the vapor front pushed the non-condensable gas (Argon) as well as other contaminations released during the heating process out of the pipe through the fill tube. Once the pipe reached isothermal temperature that can be observed from thermocouples as well as through the visualization of thermal radiation, the isothermal status was maintained for awhile to help remove the contaminants. After this "burp-off" process, the pipe was cooled down to a temperature close to the lithium melting point and then the aforementioned "burn-off" process was performed to seal the pipe. Figure 4-10B shows the heat pipe after the "burn-off" process. The hazy layer on the top of the bell jar is lithium vapor that condensed on the glass during the "burp-off" process.

Figure 4-10C shows the finished heat pipe heated by induction heater in the bell jar. The uniform thermal radiation from the fill tube (top) indicates that no condensable gas remains in the pipe. While the TZM - lithium heat pipe was successfully fabricated and tested, the power output of the current induction heater at ACT is only sufficient to push the operation temperature to 1000°C. It cannot provide enough power to reach the 1300°C target. Higher power induction heaters can provide such power. Nevertheless, the refractory metal heat pipe was considered to be the only route to realize the heat pipe based reactor concept for the two-step thermochemical cycle, and the fabrication of the refractory metal heat pipe itself is considered a major accomplishment in this program as there were many challenges that were resolved in fabrication.

(A)   (B)   (C)
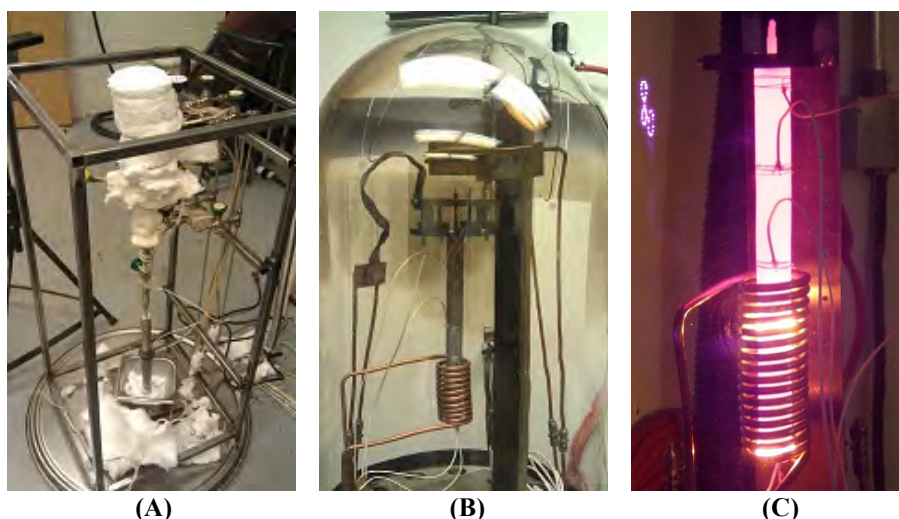
Figure 4-10. (A) Lithium cleaning and charging setup. (B) After processing (burp-off non-condensable gas) and burn-off the fill tube. (C) TZM lithium heat pipe operating in the vacuum environment.
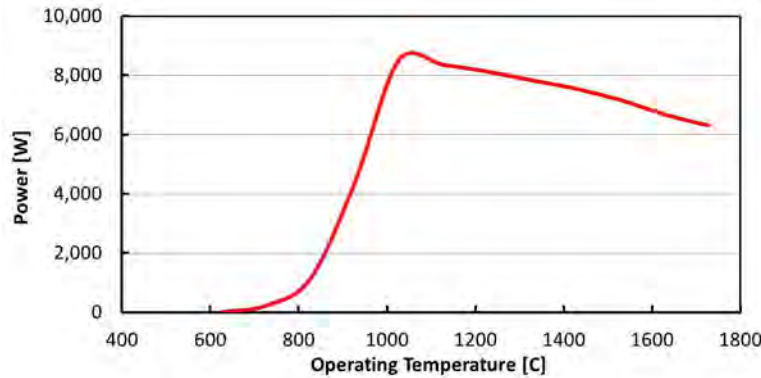
The heat transfer capability of the built TZM - Li pipe (12" x 1" assuming 8" condensation and 4" evaporator length) is about 8 kW (capillary limited) at 1300°C (Figure 4-11), estimated by ACT's heat pipe model. Higher heat transfer capability can be easily achieved by increasing the heat pipe diameter.

Figure 4-11. Estimated heat transfer capability of the TZM + Li heat pipe fabricated in this program as a function of different temperatures.

Radiative Thermal Coupling

Steady-state energy balance equations for 1-D (radial direction) heat transfer were used to estimate the temperatures of each component of the heat pipe reactor operating in a vacuum environment. The three energy balance equations are as follows:

$$Q_{in} = Q_{rad1} \text{ (Heat pipe, subscript 1)}$$
$$= Q_{rad2} \text{ (Reactor, subscript 2)}$$
$$= Q_{rad3} \text{ (Radiation Barrier, subscript 3)}$$

where the Q_{in} is equal to the thermal power from the solar receiver. The radiation heat transfer terms are listed below:

$$Q_{rad1} = \varepsilon_1 \sigma A_1 (T_1^4 - T_2^4)$$
$$Q_{rad2} = \sigma A_2 (T_2^4 - T_3^4) / [1/\varepsilon_2 + (A_2/A_3)(1/\varepsilon_3)]$$
$$Q_{rad3} = \varepsilon_3 \sigma A_3 (T_3^4 - 300^4)$$

The emissivity of the heat pipe (ε_1), the reactor (ε_2), and the radiation barrier (ε_3) was chosen to be 0.8, 1, and 0.18, respectively for the calculation. The emissivity of TZM that is typically less than 0.2 can be increased via increasing surface roughness or with the use of special coatings, for example, black rhenium coating developed by a company Ultramet.

Assuming the input thermal energy is 8 kW, and the diameter of the heat pipe, reactor, and radiation barrier are 3", 4", and 6", respectively (Figure 4-12A), the temperature of each component vs. different heat pipe/ reactor length were estimated using our 1-D calculation. The longer the heat pipe/ reactor, the larger the heat transfer area. Special care however must be taken to ensure that the heat flux is sufficient to heat the reactor to the desired temperature. Figure 4-12B shows that for heat pipe 24" long, the reactor temperature will be 1266°C and the heat pipe temperature will be 1342°C for the dimensions and input power noted here.

For an aperture diameter ~3.4" (refer to 4-3), two 24" long heat pipe reactors have A_m / A_a (area of heat transfer to area of aperture) ≈ 66, which is expected to significantly improve the heat transfer into material as discussed in Chapter 2.
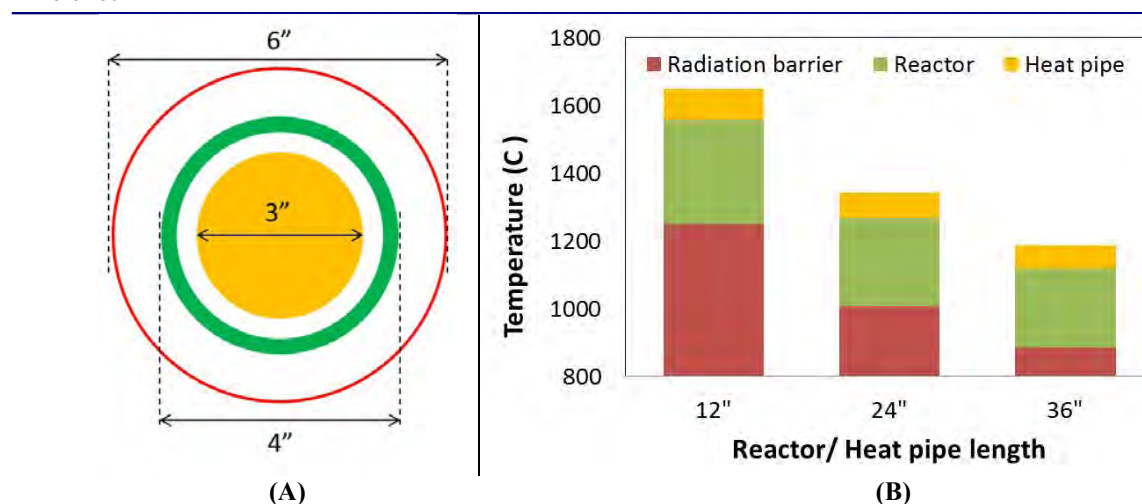
(A)   **(B)**

Figure 4-12. (A) Schematic and dimensions of the heat pipe, reactor, and radiation barrier. (B) Temperature predicted by a 1-D heat transfer calculation (assuming operating in vacuum).

4-3. Evaluation of Integration of Refractory Metal Heat Pipe Reactor into a Solar Receiver

Advanced Cooling Technologies (ACT) developed a high-temperature heat-pipe driven chemical reactor for the production of syngas from carbon dioxide and water. In the ACT design, a heat pipe provides an isothermal heat input and sink to the two steps in the metal oxide thermochemical process. In the high-temperature step, a ceria-based metal oxide is thermally reduced to produce oxygen. In the lower temperature step, the reduced metal oxide is re-oxidized by CO_2 and H_2O to produce CO and H_2, respectively, and liberate heat. The heat pipe facilitates heat addition and rejection and temperature control of the packed bed reactors. Heat input to the heat pipe reactors is provided by concentrated solar power.

ACT has investigated two temperature regimes for the two-step metal oxide thermochemical process. In the lower temperature regime heat pipes made from Haynes 230 were used at temperatures up to $1100^{o}C$ to drive the thermal reduction step ($1100^{o}C$ is the temperature limit for Haynes 230 for the operating conditions). Unfortunately, oxygen partial pressures are too low for reasonable fuels production at reactor temperatures less than $1100^{o}C$, even with the addition of other metal oxides such as zirconia to ceria, thus the decision to use refractory-metal heat pipes that can operate up to $1500^{o}C$. Higher temperatures enable higher redox extents of the ceria-based metal oxide and higher thermal efficiencies. Higher temperatures and the use of refractory metals also place demands on the solar collector system hardware and performance.

Because of the high temperatures and radiation heat loss, a high-performance dish collector was determined to be the only viable collector option. Potential design of integration of refractory metal based heat pipe based reactor into a high-performance dish collector, the design issues caused by the use of refractory metal heat pipes, and recommendations for further development are discussed.

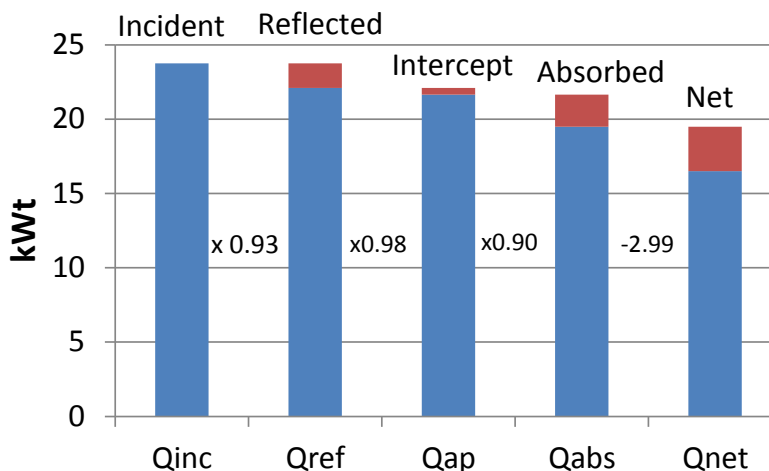### *Conceptual High Performance Dish Collector Design*
The high temperatures required for the ceria/zirconia necessitate the use of a small high-performance parabolic dish collector. The parabolic dish collector tracks the sun and most closely approximates an ideal concentrator and is the only viable collector architecture for this application. Assuming a 23.8 m^2 projected area dish with a high quality mirror system, the aperture plane flux distribution shown in Figure 4-13 is predicted. The Sandia National Laboratories CIRCE2 Solar Concentrator Optical Analysis Computer Program was used to produce Figure 4-13 [23]. The aperture diameter for optimum intercept is

about 0.086 meters (3.4 inches). The flux distribution shown in Figure 4-13 is comparable to the most accurate dish concentrators ever fielded and results in an average aperture concentration ratio of about 4000 suns.
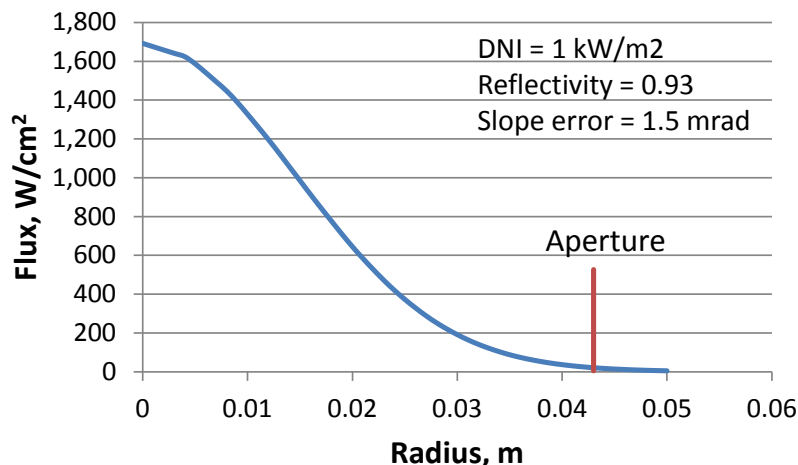
Figure 4-13. Aperture plane flux distribution for a conceptual 23.8 m² high-performance dish concentrator for the ACT refractory metal heat pipe reactors.

Assuming the above dish design, a heat pipe evaporator temperature of 1500°C, and a cavity absorptance and emissivity of 0.90, the calculated collector losses are illustrated in Figure 4-14. The net 16.4 kW is absorbed by the refractory metal heat pipe reactors in a cavity receiver. The collection efficiency is 16.4/23.8 = 68.9%.

Figure 4-14. Solar collector losses for the high performance 23.8 m² dish collector with a direct normal insolation of 1 kW/m². The losses assume a cavity absorptance and emissivity of 0.90. The radiation loss is 2.99 kW.

Conceptual Refractory Metal Heat Pipe Reactor Designs
There are several design considerations when integrating a solar reactor with concentrated solar source. One way is to insert the heat pipes into the cavity receiver. The use of a cavity decouples the process heat transfer area (heat pipe evaporators) from the radiation heat loss area (aperture). However, it is desirable that most of the flux that enters the cavity is directly incident on the heat exchanger (evaporators). Any solar flux incident on the receiver cavity walls risks overheating, minimizes cavity absorptance, and

33

increases losses. The assumed 90% cavity absorptance is a reasonable nominal value for a cavity receiver. Its actual value is not straightforward to calculate and depends on the details of the design.

Another way is to fabricate shapes other than straight cylinders. Employing spherical geometries to form a large heat pipe evaporator connected to multiple condensers makes it possible to significantly simplify reactor design and significantly increase the fraction of solar flux incident on the heat pipe evaporator/absorber.

The spherical/ dome heat pipe absorber/ evaporator geometry was developed extensively for dish/Stirling applications in the 1990s [24-26]. The spherical shape is a good match to incident flux distributions from a parabolic dish and results in relatively uniform flux distributions compared to cylindrical or conical absorber geometries. Spherical geometry heat pipe receivers proved to be very efficient and capable of handling thermal stresses over extended periods of operation. Extending these geometries to refractory metal heat pipes will be challenging, but represents the only viable route to enabling heat pipe driven packed-bed reactors to operate at the high temperatures required by ceria-based thermochemical cycles.

Figure 4-15 shows the conceptual design of the heat pipe based reactor with spherical/ dome shape evaporator operating in a vacuum chamber. The high heat flux CSP is absorbed by dome receiver/ evaporator, and then cyclically transferred to two pairs of CCHPs (total 4 heat pipes) via a PCHP. Assuming the reactor diameter is 4" and 24" long with thickness 0.5 cm, there will be ~ 1 L volume to accommodate the working material. For 80% porosity ceria powder with density is about 1.5 kg/L, 3 kg of working material is available per cycle, which requires the cycling time 78.75 sec. If $\delta = 0.03$ ($0.03*2$ / $172 = 0.00035$ g_{H2}/g_{Ceria}) and efficiency is 10%.

$$16.4 \text{ kW} * 10\% = 0.00035 \text{ } g_{H2}/g_{Ceria} * 3 \text{ kg} * 123000 \text{ J/g} * (1/t_{cycle})$$

$$t_{cycle} = 78.75 \text{ sec.}$$

The heat capacity of ceria is 390 J/kg-K; thus if there is no heat loss, 819 kJ of energy are needed to raise the temperature of 3 kg of material through a temperature swing of 700 degrees needs:

$$390 \text{ J/kg-K} * 3\text{kg} * ((1300+273)-(600+273))\text{K} = 819 \text{ kJ}$$

With 16.4 kW, the cycle time is therefore 819 kJ /16.4 kW = 50 sec. (per cycle). Therefore, the conclusion here is that the more thermal energy that goes into heating working material (ceria), the shorter the time period per cycle and the more fuel can be produced from two-step cycles.
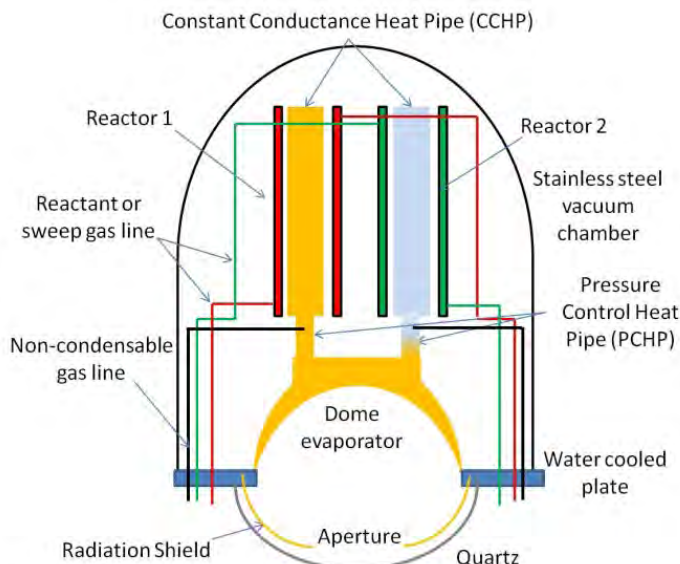
Figure 4-15. Conceptual design of refractory metal heat pipe based reactor.

Conclusions and Recommendations

The very high temperatures needed for two-step metal oxide cycles using ceria or ceria-zirconia make driving the reactions with heat pipes and packed beds extremely challenging. The required 1300°C temperatures require the use of refractory metals such as TZM. However, refractory metals are readily oxidized in air and are difficult to fabricate. To enable heat pipe driven, two-step, metal-oxide thermochemical cycles, it will be necessary to extend fabricated geometries from small-diameter, short, straight, tubular geometries to more complex shapes that can accommodate the flux distributions from parabolic dish concentrators. Even if the needed geometries can be made, it is uncertain if they can be made inexpensively enough to be economically competitive.

Thermodynamic analysis also suggests that current redox materials for two-step metal oxide cycles with a thermal reduction step require temperatures higher than those that can be accommodated by conventional heat pipes [27]. In addition to investigating new materials, to enable these temperatures, it may be necessary to either employ hybrid cycles that use a combination of heat and electricity, or use thermochemical cycles with three or more steps.

Challenges with refractory metal heat pipes further encourage more work to identify materuals that can be reduced at lower temperatures. Another option (discussed in Chapter 5 and explored here) is to use thermochemical cycles that employ three or more steps. This allows for the use of metal oxides that reduce at lower temperature along with intermediate reactants that are more readily dissociated than water or carbon dioxide and operate at less than 1000°C.

5. A New Low-Temperature Four-Step Thermochemical Cycle for Water or CO$_2$ Splitting

A key objective for the two-step ceria cycle was to screen different doped ceria materials (i.e., Zirconium, Praesodymium) with the intent to identify a promising doped material that would enable thermal reduction of ceria at temperatures less than 1100°C. Based on detailed calculations and experiments performed by Professor Haile's team at Caltech, the minimum temperature for the endothermic thermal reduction step (using Zr-doped ceria) was determined to be 1300°C. These results are described in Chapter 3.

Based on this results (discussed in detail in the continuation report), a decision was made to focus year two of the program on a high temperature reactor design that can accommodate high temperature operation (1300°C). As shown in Phase I, superalloy-based heat pipes can be used up to 1100°C, but not at higher temperature due to concerns with thermal creep. As such, our focus in year two has been on the development of a refractory metal heat pipe based reactor; this is described in Chapter 4. In parallel, options for lower-temperature operation were explored. The results of this effort are described in Chapter 5.

The end-result is a new four step thermochemical cycle for water and/or CO$_2$ splitting that can be performed at temperatures < 1000°C. This cycle was proposed by Dr. Rich Diver and, unlike other multi-step thermodynamic cycles, it does not involve the use of any toxic or corrosive materials. The reaction scheme was initially proposed by Dr. Richard Diver, a consultant on this SBIR program. Since then, efforts have been made at ACT with support from Rowan University to test the scheme. ACT further filed a patent on this new cycle with the U.S. Patent and Trademark Office in July, 2014.

Before describing the details of the cycle, the basic idea is to use a metal oxide that can be thermally reduced at T < 1000°C such as Co$_3$O$_4$. The products are 3CoO + 1/2O$_2$ as shown in the equilibrium calculation plotted in Figure 5-1 below.
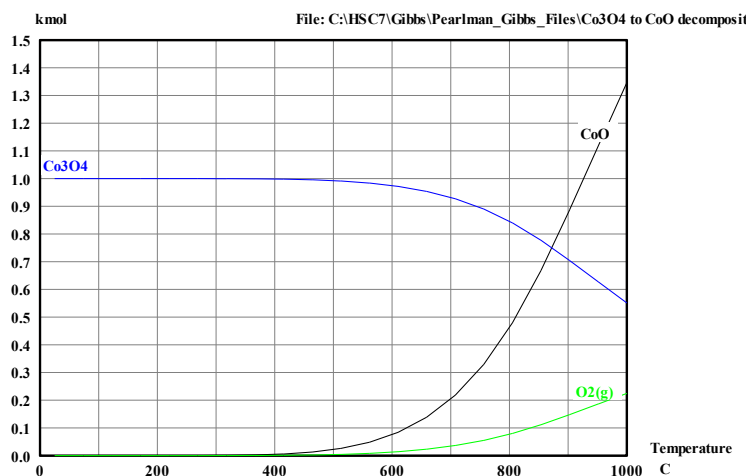
Figure 5-1. Thermal Reduction of CO$_3$O$_4$ to CoO and Oxygen gas at T < 1000°C [HSC Calculations].

Then, an intermediate oxygenated species (rather than directly splitting water or CO$_2$) can be used to re-oxidize the reduced metal oxide, producing other intermediates that are used in subsequent reaction steps. The final net reaction is that for water or carbon dioxide splitting, i.e., H$_2$O $\rightarrow$ H$_2$ + 1/2O$_2$ or CO$_2$ $\rightarrow$ CO + 1/2O$_2$. Conveniently, three of the four steps in the new thermochemical cycle are standard industrial processes, which lends itself to commercialization, so long as the new fourth step is thermodynamically

and kinetically favorable. The new step involves the re-oxidation of the reduced metal oxide with an oxygenated fuel, such as methanol or even syngas having CO, to produce an intermediate, methane (CH_4). Notably, $3CoO + CH_3OH \rightarrow Co_3O_4 + CH_4$. Here, methanol is converted to methane and the oxygen from the methanol refills the vacancies in the reduced CoO to form Co_3O_4. In this chapter, the thermodynamic basis for this and similar thermochemical cycles are presented along with limited experimenstal results demonstrating feasibility. In short, preliminary flow reactor studies have shown that reduced cobalt oxide and methanol produce methane, yet the cycle has to be repeated to ensure that the reduce oxide is re-oxidized in the process. Key issues and opportunities are discussed herein.

5-1. Background and Thermodynamics Analysis on Low-temperature Thermochemical cycles

Most of the energy consumed in the world today is "stored solar energy" in the form of fossil fuels such as petroleum, natural gas, and coal. Fossil fuels, however, are finite and their combustion has led to an increase in the amount of carbon dioxide in the atmosphere and other pollutants in the environment. Their limited availability also has national security and economic implications. Solar and nuclear energy are the world's only viable long-term energy options and fuels production from these sources is potentially an environmentally advantageous, long-term alternative to fossil fuels.

To split water and produce hydrogen gas, more than 200 thermochemical cycles have been proposed. Much effort was invested in the 1970's during the oil crisis with efforts continuing albeit at a reduced level. Regardless, multistep thermochemical cycles for the production of fuels from water and/or carbon dioxide at temperatures less than $1000^{o}C$ is highly desirable noting that heat from nuclear facilities can be used to drive these cycles. Alternatively, two-step metal oxide cycles that alternately thermally reduce a metal oxide such magnetite (Fe_3O_4) to wustite (FeO), producing oxygen, and then reoxidize the metal oxide with water or carbon dioxide to produce hydrogen or carbon monoxide have also been proposed. Here, the metal oxide is cycled between the high temperature thermal reduction step and a lower temperature oxidation step. The disadvantage of the two-step cycles (as discussed in this Final Report, Chapter 2) is their need for very high temperatures ($\approx 1300 \sim 1500^{o}C$) for thermal reduction. While their simplicity is attractive, the associated high-temperature materials and thermal issues makes them challenging. Two-step cycles are discussed below followed by the new four step thermochemical cycle developed in this Phase II program.

Two-Step Thermochemical Cycles
The high temperature required for two-step cycles are a result of the need to perform the two reactions under favorable conditions ($\Delta G < 0$, Figure 5-2). These constraints lead to the need for the two reactions (thermal reduction and re-oxidation) to be carried out at different temperatures. The temperature difference between the two reactions and the reaction entropy changes determine the range of favorable conditions. However, because the change in entropy of thermal reduction of metal oxides is primarily from oxygen evolution, entropy changes are inherently limited and the temperature difference between reactions needs to be over $1000^{o}C$ [26]. While it is possible to shift the curves to the left by altering the reactant chemistry, i.e., doping with other oxides, the slopes of the curves (entropy changes) cannot be appreciably altered. Reducing the pressure for the thermal reduction reaction by the use of a vacuum or inert sweep gas can lower the thermal reduction temperature. However, pressure manipulation has negative thermodynamic consequences and is inherently limited. The use of a sweep gas necessitates an expensive separation step and efficient gas-to-gas recuperation to minimize the thermal losses from heating the sweep gas. The high temperatures required for metal oxide cycles also preclude the use of nuclear power, place challenging demands on materials, and severely impact the design and efficiency of solar collection hardware.
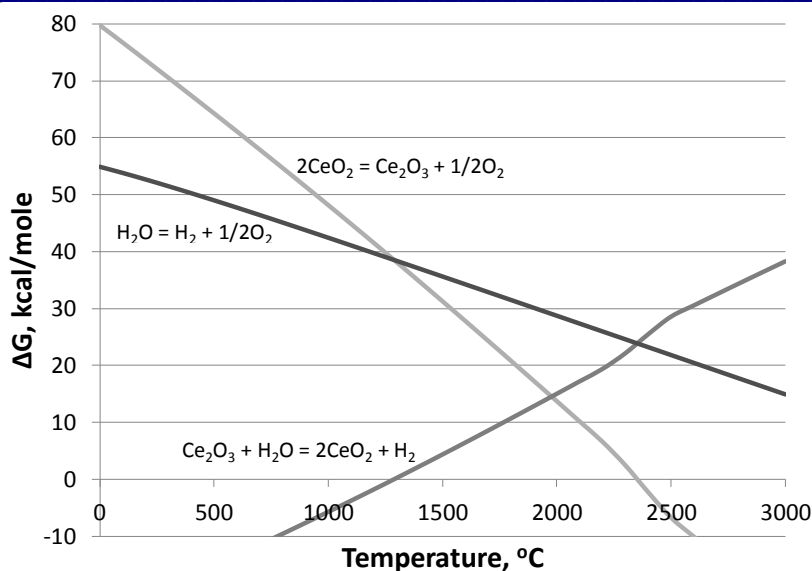
Figure 5-2. Thermodynamics of the two-step cerium oxide water splitting cycle showing the temperature swing between reduction and re-oxidation of the metal oxide.

As discussed in Chapter 2, efforts to dope the ceria material were successful at reducing the temperature needed for thermal reduction yet not below $1000^{o}C$ while maintaining reasonable efficiency. To enable lower temperature operation, thermochemical cycles with more than two steps have been studied such as the decomposition of sulfuric acid, with the Sulfur-Iodine and Hybrid Sulfur processes receiving most of the attention.

Multistep Thermochemical Cycles

By breaking the overall water or carbon dioxide splitting thermochemical cycle into more than two steps, the temperature difference between steps can be proportionally decreased. For the metal oxide redox reaction, reoxidizing a metal oxide with an intermediate oxide that is more readily reduced than water or carbon dioxide offers an opportunity to decrease the temperature difference between the reduction and reoxidation reactions. This allows the use of metal oxides that can be thermally reduced at lower temperatures than magnetite or ceria. For example, cobalt oxide (Co_3O_4) can be reduced at less than $1000^{o}C$ with the product and reactants in their standard state. The reduced cobalt oxide (CoO) is not capable of being reoxidized by water or carbon dioxide. *However, reduced cobalt oxide is thermodynamically capable of being reoxidized by methanol, which has an oxygen binding Gibbs free energy about half that of water.* [27.66 kcal/mole for $CH_3OH(l) \rightarrow CH_4(g) + 1/2O_2(g)$ vs. 56.68 kcal/mole for $H_2O(l) \rightarrow H_2(g) + 1/2O_2(g)$, both at $25^{o}C$.] The hematite/magnetite ($3Fe_2O_3/2Fe_3O_4$) metal oxide reaction is also viable. The water splitting cycle is completed with a second endothermic oxidation reaction and recycling some of the oxidation products back to the intermediate oxide, e.g. methanol. Because the methane reforming reaction produces an extra mole of hydrogen or carbon monoxide compared to what is needed to synthesize methanol, the net reaction is the production of hydrogen and/or carbon monoxide from water and/or carbon dioxide.

Table 5-1 illustrates the new Metal Oxide cycle for water splitting in which the water and methanol are assumed to stay in the gas phase. Furthermore, Table 5-2 illustrates the same scheme applied for carbon monoxide production from carbon dioxide. In some cases, modifications to the scheme can further be used to synthesize fuel, such as the synthesis of methanol shown in Table 5-3. In this example, carbon dioxide and water are fed in step 3 at a ratio of two moles of H_2O per one mole of CO_2. The reaction schemes illustrated in Tables 5-1 to 5-3 show that by adjusting the relative amounts of carbon dioxide and

water fed into steps 3 or 4, it is possible to produce syngas with any ratio of CO to H_2 desired or produce methanol!

Table 5-1. Reactions in the four-step Metal Oxide cycle in which hydrogen is the product fuel.

Step	Reaction	ΔH, kcal @25°C	Temperature, ^{o}C
1	$Co_3O_4 \rightarrow 3CoO + 1/2O_2$	46.89	>800°C
2	$3CoO + CH_3OH \rightarrow Co_3O_4 + CH_4$	-16.68	<300°C
3	$H_2O + CH_4 \rightarrow CO + 3H_2$	49.21	>800°C
4	$CO + 2H_2 \rightarrow CH_3OH$	-21.62	200 ~ 300°C
Net	$H_2O \rightarrow H_2 + 1/2O_2$	57.8	

Table 5-2: Reactions in the four-step Metal Oxide cycle in which carbon monoxide is the product fuel.

| Step	Reaction	ΔH, kcal @25°C	Temperature, ^{o}C
1	$Co_3O_4 \rightarrow 3CoO + 1/2O_2$	46.89	>800°C
2	$3CoO + CH_3OH \rightarrow Co_3O_4 + CH_4$	-16.68	<300°C
3	$CO_2 + CH_4 \rightarrow 2CO + 2H_2$	59.04	>800°C
4	$CO + 2H_2 \rightarrow CH_3OH$	-21.62	200 ~ 300°C
Net	$CO_2 \rightarrow CO + 1/2O_2$	67.63	

Table 5-3. Reactions in the four-step Metal Oxide cycle in which methanol is the product fuel.

Step	Reaction	ΔH, kcal @25°C	Temperature, ^{o}C
1	$3Co_3O_4 \rightarrow 9CoO + 3/2O_2$	140.67	>800°C
2	$9CoO + 3CH_3OH \rightarrow 3Co_3O_4 + 3CH_4$	-50.04	<300°C
3	$CO_2 + 2H_2O + 3CH_4 \rightarrow 4CO + 8H_2$	157.46	>800°C
4	$4CO + 8H_2 \rightarrow 4CH_3OH$	-86.48	200 ~ 300°C
Net	$CO_2 + 2H_2O \rightarrow CH_3OH + 3/2O_2$	161.61	

The thermodynamics of the Metal Oxide cycle for carbon dioxide splitting (Table 5-2) is illustrated in Figure 5-3. The cobalt oxide thermal reduction reaction in step 1 can be performed at 980°C with the products and reactants at their standard state and in air at temperatures down to about 940°C. The thermal reduction temperature can be lowered to near 800°C by using an inert sweep gas such as nitrogen or steam. By comparison, to thermally reduce cerium oxide ($2CeO_2 \rightarrow Ce_2O_3 + 1/2O_2$) with products and reactants at their standard states requires temperatures in excess of 2300°C (see Figure 5-1). Similarly, the reduction of magnetite to wustite ($Fe_3O_4 \rightarrow 3FeO + 1/2O_2$) requires temperatures in excess of 2700°C!

Here, in this multistep mechanism, the reduced cobalt oxide is thermodynamically capable of being reoxidized by methanol to produce methane at temperatures less than about 380°C ($3CoO + CH_3OH \rightarrow CH_4 + Co_3O_4$). The methane produced is subsequently reformed with water and/or carbon dioxide using solar or nuclear heat input to produce carbon monoxide and hydrogen, part of which is synthesized back to methane in steps 4 and 2. Because methane reforming produces an extra mole of hydrogen or carbon monoxide compared to what is needed to synthesize methane, the net reaction is the production of hydrogen and/or carbon monoxide.

Steps 1, 3, and 4 in Tables 5-1 to 5-3 are well established processes, with steps 3 and 4 industrial processes. In fact, solar reforming of natural gas, step 3, of which methane is the main constituent, has recently been shown to be a viable approach for storing solar energy in chemical form.
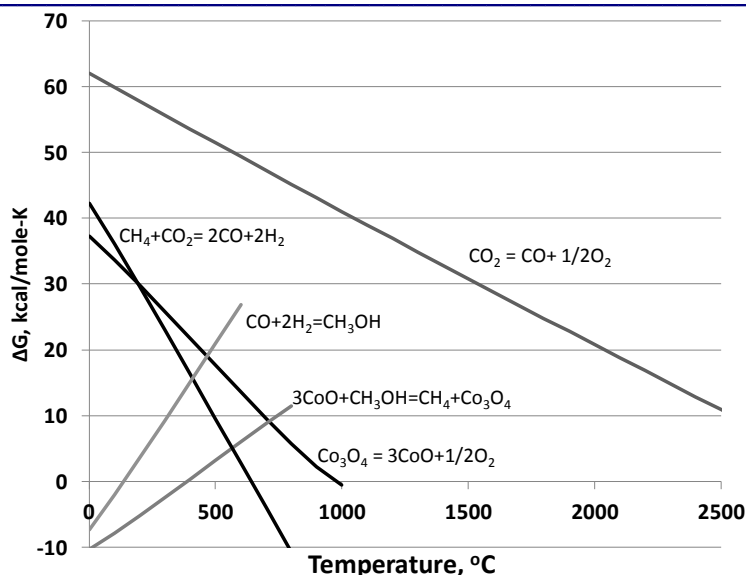
Figure 5-3. Thermodynamics of the four-step Metal Oxide carbon dioxide splitting cycle.

All of the products and intermediate reactants in Tables 5-1 to 5-3 are readily separable. Oxygen gas produced in step 1 can be easily separated from the solid reduced metal oxide. In addition, unlike the high-temperature two-step metal oxide cycles, the metal oxide reduction reaction can potentially be performed in air. The relatively low temperatures also enable the use of reactors constructed from conventional metals. Methane gas produced in step 2 can be readily separated from the liquid methanol feed and solid metal oxide. Alternatively if step 2 is performed with methanol in the gas phase, any methanol carried over can be easily separated from methane by condensation. Step 3 requires no separations and any recycle in step 4 (of Tables 5-1 to 5-3) can be readily separated by condensation and is standard practice. Heat for steam generation needed for step 3 or for a steam sweep gas to help drive step 1 is available from steps 2 and 4.

The efficiency of these Metal Oxide cycles is also potentially high. A simplified state point efficiency analysis for carbon monoxide production from CO_2 is illustrated in Table 5-4 and Figure 5-4. The analysis assumes cobalt oxide reduction (step 1) at $900^{\circ}C$; steam reforming of methane (step 3) at $800^{\circ}C$; and metal oxide re-oxidation and methanol synthesis (steps 2 and 4) at $300^{\circ}C$. The cycle efficiency is 63.8%, assuming complete conversion and full recuperation of sensible heat from the reduced cobalt oxide and reformed syngas. Even with no heat recuperation, the cycle efficiency is 46.9%, also assuming complete conversion.

Table 5-4. Efficiency Analysis for Carbon Dioxide Splitting Metal Oxide Cycle

State	Composition	Temp, °C	H, kcal	Process	ΔH, kcal
			Metal Oxide - Methanol Cycle Analysis		
1	Co_3O_4	300	-207.995		
2	Co_3O_4	900	-180.036	Sensible heating of Co_3O_4	27.959
3	3CoO	900	-136.137		
4	$1/2O_2$	900	3.443	Step 1- Thermal reduction	47.342
5	3CoO	300	-159.978	Sensible cooling of 3CoO	-23.841
6	$1/2O_2$	25	0	Sensible cooling of $1/2O_2$	-3.443
7	$3CoO + CH_3OH$	300	-204.427		
8	$Co_3O_4 + CH_4$	300	-223.003	Step 2 - Reoxidation	-18.576
9	$CH_4 + H_2O$	300	-70.527		
10	$CH_4 + H_2O$	800	-58.101	Sensible heating	12.426
11	$CO + 3H_2$	800	-4.275	Step 3 – CH_4 reforming	53.826
12	$CO + 3H_2$	300	-18.796	Sensible cooling	-14.521
13	CO_2	25	-94.05		
14	CO_2	300	-91.265	CO_2 preheating	2.785
15	$CO_2 + 3H_2$	300	-85.583		
16	$CH_3OH + H_2O$	300	-99.968	Step 4 -Methanol synthesis	-14.386
17	CO	300	-24.478	Product CO	
18	CO	25	-26.42	Product CO cooling	-1.942
Net	$CO_2 \rightarrow CO+1/2O_2$				67.629
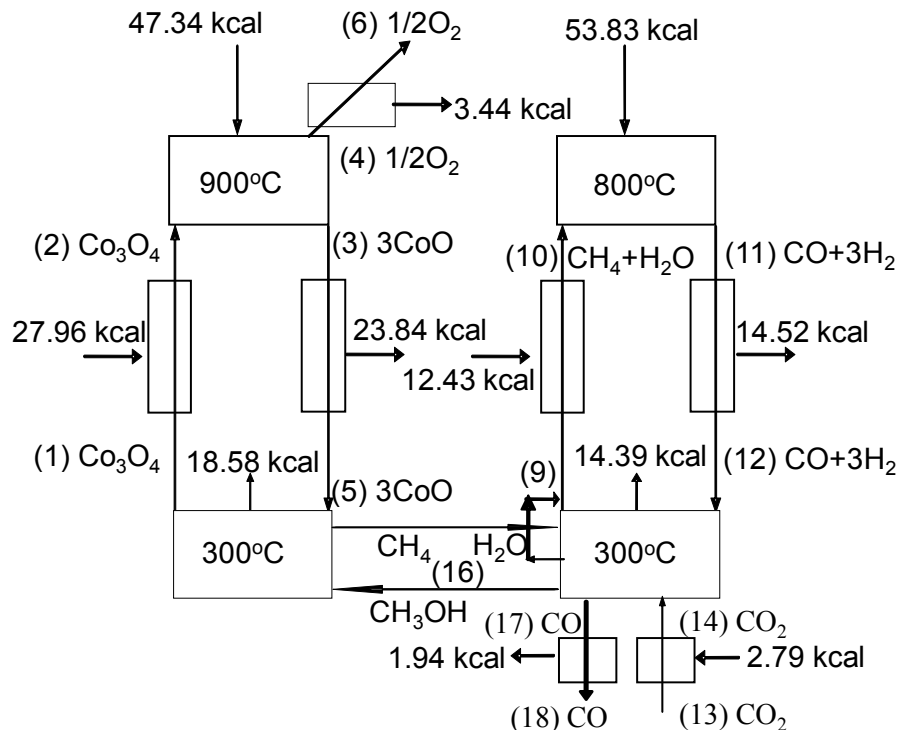
Figure 5-4. Simplified Metal Oxide cycle efficiency analysis for the CO₂ efficiency analysis in Table 5-4. Numbers in parenthesis corresponds to the state points in Table 5-4.

Key Issues in the New Thermochemical Cycles

All of the steps in the Metal Oxide Cycle s are thermodynamically feasible, yet performing step 2 at a reasonable reaction rate while avoiding side reactions is critical. To improve the thermochemical potential for the desired reaction and minimize the likelihood of side reactions, it is necessary to perform reaction 2 at a low temperature. The introduction of a catalyst may help reaction kinetics, but are likely to promote side reactions that form water or carbon dioxide rather than reoxidize the metal oxide. The classic methanation reaction in which syngas forms methane and water is most likely. On the other hand, the kinetics of the metal oxide reoxidation reaction and oxygen transport within the bulk oxide favor elevated temperatures.

It is noteworthy that methanol synthesis (reaction 4 in Tables 5-1 to 5-3) thermodynamically favors similar potential side reactions as step 2, i.e., forming CO_2 or H_2O. Figure 5-5a shows equilibrium calculations for conventional methanol synthesis. However, with the use of a catalyst, commercial methanol synthesis is able to avoid CO_2 and H_2O side reactions. Figure 5-5b shows the same thermodynamic equilibrium conditions as Figure 5-5a with the exception of excluding carbon dioxide or water formation. Figure 5-5b closely represents the methanol synthesis process in commercial practice.
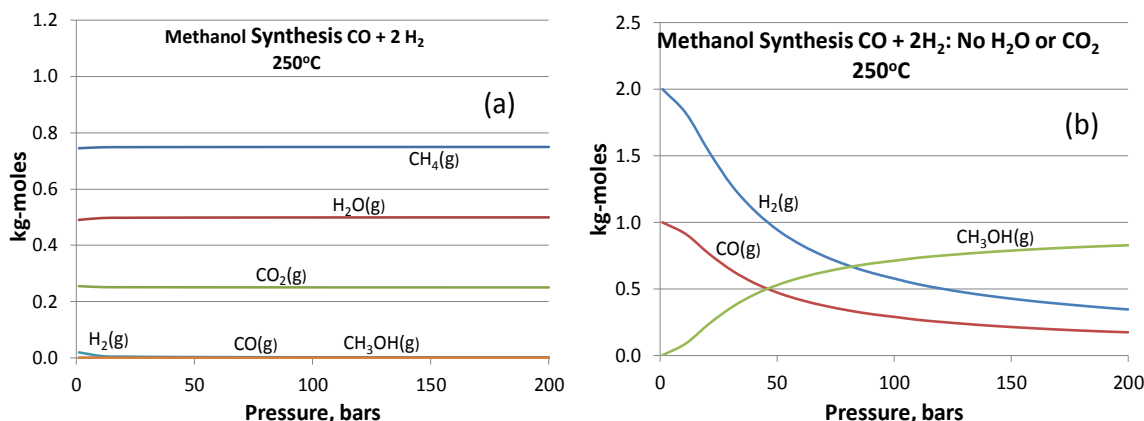

Figure 5-5. Equilibrium thermodynamic calculations for conventional methanol synthesis (a) with and (b) without CO_2 or H_2O as a potential reaction products. Methanol production using selective catalysts closely match the results in (b).

If side reactions can be avoided in step 2 in Tables 5-1 to 5-3 as in conventional methanol synthesis, thermodynamic calculations show similar possibilities. Analogous to Figure 5-4, Figure 5-6 shows similar results and the potential for driving step 2 as desired.
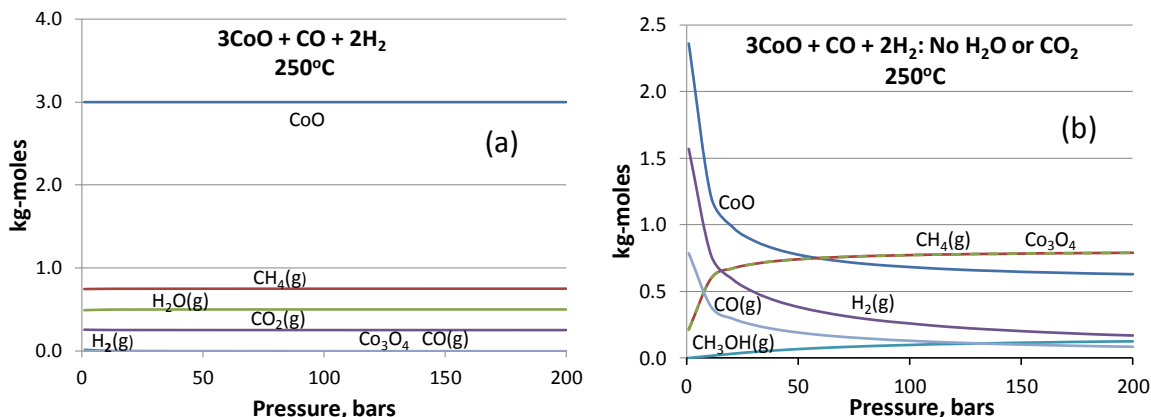

Figure 5-6. Thermodynamics of metal oxide-methanol reduction reaction assuming equilibrium (a) and equilibrium assuming no CO_2 or H_2O as a potential reaction products (b).

42

5-2. Preliminary Experimental Work

After developing the thermochemical cycles described above, a key technical challenge is to demonstrate the feasibility of step 2, $3CoO + CH_3OH \rightarrow Co_3O_4 + CH_4$. There are two key issues that need to be demonstrated: (1) the re-oxidization of the reduced oxide using methanol and (2) the production of methane without substantial contributions from side reactions such as those producing water, carbon dioxide, etc. which are at the heart of what we are trying to split!

To demonstrate feasibility, two initial studies were performed: (1) using nickel doped iron oxide and (2) using doped cobalt oxides. In the first study, Ni-doped iron oxide (Fe_2O_3) was prepared having the chemical composition $Fe_{2.4}Ni_{0.6}O_4$ as confirmed using XRD (at Rowan University). The sample was prepared using 9.5 g Fe_2O_3 to which 0.5 g of nickel nitrate was added along with 100 mL DI water. HNO_3 was also added in sufficient quantity to adjust the pH = 3. The solution was stirred overnight and dry to obtain the $Fe_{2.4}Ni_{0.6}O_4$ powder.

A flow reactor was then fabricated from stainles-steel (Figure 5-7). An 8.6 g sample of $Fe_{2.4}Ni_{0.6}O_4$ powder was inserted and tested. The entire reactor assembly was then heated using a SiC ceramic heater (shown on the right-side of the flow reactor, left figure). To reduce the material, the reactor was heated to $650^{\circ}C$ with an Argon sweep having a flowrate of 30 cc/s (1800 sccm). Since thermal reduction of iron oxide is negligible at $650^{\circ}C$, as shown in the HSC equilibrium calculation in Figure 5-8, a 5% vol. H_2-Ar flow was used to chemically reduce the oxide.
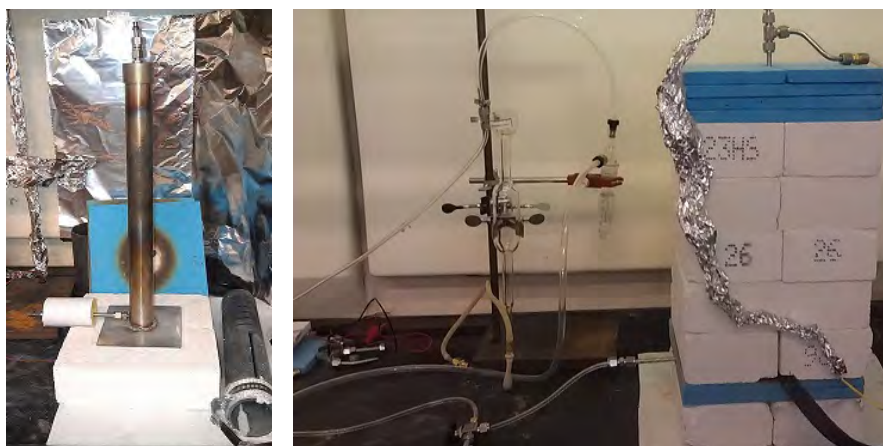

Figure 5-7. Flow reactor shown on the left inserted in SiC heater element surrounded by high-temperature insulation shown on the right.
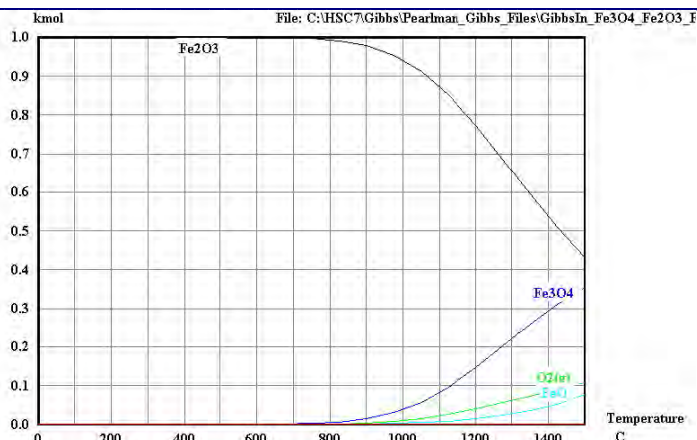
Figure 5-8. HSC calculation for thermal reduction of iron oxide (Fe₂O₃) as a function of temperature.

After reduction, the material was re-oxidized at 300°C and 1 atm with methanol (Ar at 14 cc/s bubbling through liquid methanol, ≈ 13% vol methanol). 500 ml gas samples were taken every minute and analyzed using an SRI GC. Results (Figure 5-9) clearly show the presence of methane in the effluent. Side reactions also contribute the presence of water and hydrogen gas. To maximize the methane production while minimizing the side reactions, additional studies are needed. In addition, repeat studies are needed to definitively demonstrate that the reduced oxide is re-oxidized with methanol, a requirement for the thermochemical cycles shown in Tables 5-1 to 5-3 to be closed.
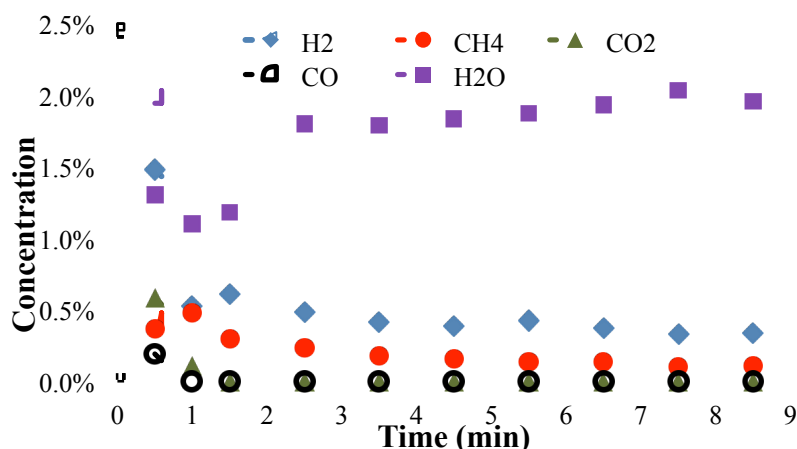
Figure 5-9. Methane, water, H2, CO₂ and CO in the effluent composition of a Ni-doped iron oxide material with a 13%vol. methanol and argon flow.

For completeness, one general question with the above results involves the use of hydrogen to chemically reduce the doped iron oxide, which was done here since the heater temperature was limited. The oxide was undoubtedly reduced but may have, in part been reduced to the parent metal (Fe) rather than to FeO and/or Fe₃O₄. Additional studies are therefore now being performed at ACT using a modified high pressure flow reactor on loan from Rowan University.

Summary
A new family of thermochemical cycles based on a methanol-methane cycle is proposed as a way to split water at T < 1000°C using solar or nuclear power. The cycles employ two high-temperature endothermic reactions and an intermediated hydrocarbon oxide, such as methanol. Because the oxygen binding energy

of methanol is approximately half that of water or carbon dioxide, the temperature requirements of the high-temperature endothermic steps are greatly reduced compared to water or carbon dioxide splitting. The other half of the thermal requirement is applied to the oxidation of methane in a conventional methane reforming reaction. Solar reforming of methane offers a near-term opportunity for storing solar energy in the form of chemical energy. In the long term the reduction of the oxygenated hydrocarbon to produce methane would, in principle, eliminate the need for the natural gas feedstock and enable hydrocarbon fuels production using only carbon dioxide, water, and solar or nuclear power inputs.

The key to the new cycle is the reduction of the hydrocarbon oxide such as methanol to produce methane. While methane-to-methanol conversion is both standard practice and the subject of a significant amount of research, methanol-to-methane has received much less attention. With that said, however, our initial experimental results look promising as methane was measured in the effluent from a high-temperature flow reactor developed at ACT used to access feasibility of step 2. Now, repeat cycles need to definitely be demonstrated. There are also several other unexplored options for methanol-to-methane conversion, including thermochemical, electrochemical, photochemical, or hybrid approaches. These are outside of the scope of this work but pose interesting options for follow-on studies.

6. Future Work and Commercialization Efforts

## 6-1. Reactor Design for Two-step Metal Oxide Based Cycle

A refractory metal heat pipe for use in a solar fuel reactor was successfully built during this program, yet challenges remain for the refractory metal heat pipe based reactor design. According to the analysis performed by Diver Solar, LLC, the dome shape receiver/ evaporator is the most efficient receiver design for the integration between the heat pipe reactor and the solar receiver. This requires the receiver to be fabricated using refractory metals, which is technically feasible but has not been performed yet. In addition, the PCHP made by refractory metal and the integration with refractory metal CCHPs and a PCHP also needs to be worked out for the realization of the heat pipe reactor. In spite of several challenges remaining, the refractory metal based reactor design can efficiently deliver the heat into working material to maximize the conversion efficiency, and perform thermal cycling without moving parts. Those features are still very attractive in terms of realizing two-step metal oxide based thermochemical cycles.

6-2. Material Study for Multi-step Thermochemical Cycle

The possibility of a lower temperature cycle developed during this program also offers significant potential as it alleviates the structure material challenges and (as described in Chapter 5) relies on the use of three commercial reaction steps employed on large scales. However, more work needs to be done to demonstrate feasibility of step 2. While the preliminary tests show methane formation using methanol to re-oxidize the reduced metal oxide (cobalt oxide in this case), the repeatability of the cycle needs to be demonstrated to clearly show that reduced metal oxide can be re-oxidized. Since the thermodynamics analysis (Figure 5-6) shows the reaction is favored in higher pressure conditions, a BTRS (Bench Top Reactor Systems) system that can performed high pressure tests (up to 30 bar) has been borrowed from Rowan University (Figure 6-1) to continue the material study at ACT. Three potential working material candidates, Ni-doped cobalt oxide, Zn-doped cobalt oxide, and Cu-doped cobalt oxide were prepared by Rowan University. Initial tests using Zinc doped Cu did show methane formation using methanol and reduced cobalt oxide and oxygen gas was released during the second cycle of the high temperature reduction process. These results suggest that the reduced metal oxide has successfully re-oxidized the reduced cobalt oxide, a key requirement for the step to work (Figure 6-2). A more rigorous study showing that the cobalt oxide can be reduced and re-oxidized with methanol over multiple cycles is needed. These tests are beyond the scope of the original work proposed to DOE but are now ongoing at ACT to conclusively demonstrate the reduced temperature mechanism described in Chapter 5.

(A) (B)
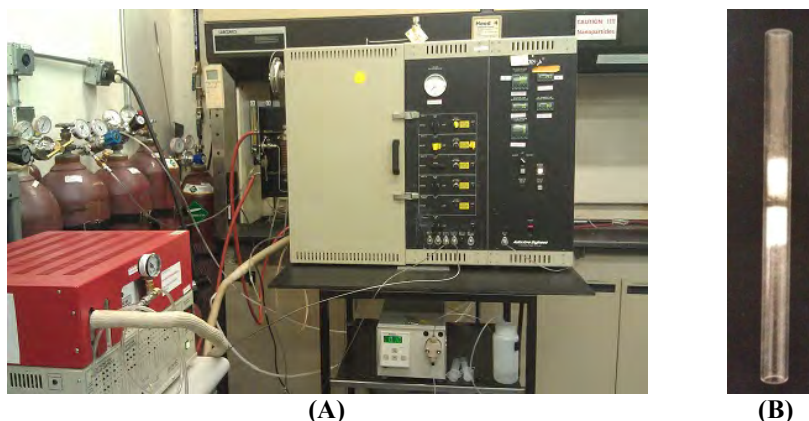
Figure 6-1. (A) Experimental setup for methane-methanol conversion material studies. (B) 30 mg Zinc doped Cobalt oxides in quartz reactor.

(A)   (B)
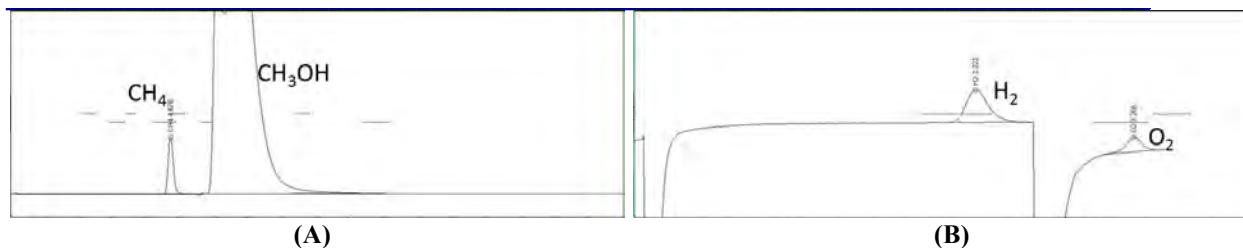
Figure 6-2. (A) Methane formation during the re-oxidation step of the cycle - step 2 (FID signal). (B) Oxygen released during the second thermal reduction step - second cycle (TCD signal). Note that some H_2 is observed during the second reduction step and may come from the decomposition of CH_3OH that either remained in the reactor or in the liquid fuel transfer line.

6-3. Commercialization Efforts

To help commercialize the technology developed in this program, ACT has been working with Dawnbreaker. In year 1 of the project, a primary market research report was developed highlighting feedback received from industry and government representatives. The report shows that there is significant interest in the technology yet to be cost competitive with alternative strategies for generation of syngas, e.g., steam methane reforming, necessary government policies related to carbon emissions and the continued use (and even recent expansion of natural gas exploration) must be addressed. In short, it is extremely difficult for new renewable technologies for hydrogen or syngas production to be cost competitive with existing commercial-scale technologies for syngas production that rely on the use of fossil fuels unless appropriate government policies are in place to curtail carbon emissions and the continued use of relatively inexpensive fossil fuels. In year 2 of the program, we have continued working with Dawnbreaker. They helped to identify key network contacts in companies that include Air Products and Chemicals, Air Liquide, Praxair, and others, with whom are following up.

At ACT, we have also been considering options for scaling up the reactor design and applying the technology developed in this program to new applications for which licensing opportunities may be available. For example, we have been considering the use of embedded high-temperature heat pipes into a packed bed reactor to enhance heat transfer inside the bed and achieve isothermalization. Many chemical processes including air separation for example (noting that most of the large industrial gas manufacturers have some stake in air separation technologies) may benefit from this technology, which is in effect a technology transfer of work done in this program to other applications. One specific recent effort has been to explore the use of heat pipes to improve the Ceramic Autothermal Recovery process of the BOC group (now part of Linde group) for air separation. Another opportunity that we are looking into is in the area of high temperature metal oxide based thermal storage developed by General Atomics. Lastly, other opportunities that can benefit from the integration of heat pipes into solar receivers include recent efforts to combine solar heating to drive chemical processes such as coal gasification and methanol synthesis.

7. References and Patent Application Resulting from this Program

[1]   Pearlman, H., Chen, C.H. (2012) "Syngas production by thermochemical conversion of CO_2 and H_2O using a high-temperature heat pipe based reactor," Solar Hydrogen and Nanotechnology VII, Proceedings of the SPIE, Vol. 8469 (2012).

[2]   Hao, Y., Chueh, W., and Haile, S., "Thermochemical Water Splitting with Zirconium-Substituted Cerium Oxides," 2012 PRiME Meeting, The Electrochemical Society, MA2012-02, 14, 1823, in the session Fuel Production from Renewable Sources - Oct 11 2012

[3]   A full patent was filed with the USPTO on the cycle described in Chapter 5, "System and process for producing fuel with a methane thermochemical cycle." U.S. Application No.: 14/445,492 System and Process for Producing Fuel with a Methane Thermochemical Cycle, Filing Date: July 29, 2014.

[4]   Diver, R., Miller, J. (2013) "New Low-Temperature Methane Thermochemical Cycles for Sustainable Fuels Production," Prepared and ready for journal submission.

8. References

[1]   Song, C, "Global challenges and strategies for control, conversion and utilization of CO_2 for sustainable development involving energy, catalysis, adsorption and chemical processing," Catalysis Today 115, 2-32 (2006).

[2]   Abanades, S, Charvin, P, Flamant, G, Neveu, P, "Screening of water-splitting thermochemical cyces potentially attractive for hydrogen production by concentrated solar energy," Energy 31, 2805-2822 (2006).

[3]   Chueh, W, Falter, C, Abbott, M, Scipio, D, Furlur, P, Haile, 5, Steinfeld, A, "High-Flux Solar-Driven Thermochemical Dissociation of CO_2 and H_2O Using Nonstoichiometric Ceria," Science 330, 1797-1801 (2010).

[4]   Panlener, R. J, Blumenthal, R. N. & Gamier, J. E, "A Thermodynamic Study of Nonstoichiometric Cerium Dioxide," J. Phys. Chem. Solids 36, 1213-1222 (1975).

[5]   Chueh,W; Haile, S, "A thermochemical study of ceria: Exploring an old material for new modes of energy conversion and CO_2 mitigation," Philosophical Transaction of the Royal Society 368, 3269-3294 (2010).

[6]   Furler, P., Scheffe, J., and Aldo Steinfeld, A., "Syngas production by simultaneous splitting of 1420 and CO2via ceria redox reactions in a high-temperature solar reactor," Energy Environ. Sci. 5, 6098-6 103 (2012).

[7]   Diver, R., Siegel, N., Moss, T., Miller, J., Evans, L., Hogan, R., Allendorf. M., Stuecker, J., James, fl, "Innovative Solar Thermochemical Water Splitting," Sandia Report SAND2008-0878 (2008).

[8]   Kaneko, H., Miura, T., Fuse, A., Ishihara, H., Taku, S, Fukuzumi, H., Naganuma, Y, and Tamaura, Y., "Rotary- Type Solar Reactor for Solar Hydrogen Production with Two-step Water Splitting Process," Energy Fuels 21(4), 2287-2293 (2007).

[9]   Bernard M. Abraham, Felix Schreiner, Alan Attia , and Anthony Jeanotte, "A Promising Thermochemical Cycle for Splitting Water"
      http://web.anl.gov/PCS/acsfuel/preprint%20archive/Files/21_3_NEW%20YORK_04-76_0031.pdf

[10] Computer program, "Outokumpu HSC Chemistry for Windows", 2002, Version 5.1 (HSC 5), Antti Roine, 02103-ORC-T, Pori, Finland.

[11] Walker, K., Hartenstine, J, Tarau, C., Sarraf, fl, and Anderson, W., "Low-Temperature, Dual Pressure Controlled Heat Pipes for Oxygen Production from Lunar Regolith," 15th IHPC, Clemson, USA (2010).

[12] Martini, W. R., "Stirling Engine Design Manual," NASA CR-135382 Final Report (1978).

[13] R. J. Panlener, R. N. Blumenthal, J. E. Garnier, "A Thermodynamic Study of Nonstoichiometric Cerium Oxide", J. Phys. Chem. Solids, **36**, 1213 (1975).

[14] W. C. Chueh and S. M. Haile, "A Thermochemical Study of Ceria: Exploiting an Old Material for New Modes of Energy Conversion and CO2 Mitigation," Phil. Trans. R. Soc. **368**, 3269-3294 (2010).

[15] HSC Chemistry 5.11 software, Outokumpu Research Oy, Pori, Finland, A. Roine.

[16] Chiba, R.; Taguchi, H.; Komatsu, T.; Orui, H.; Nozawa, K.; Arai, H. Solid State Ionics **2011**, 197, 42–48.

[17] Zhang, J.; Von Dreele, R. B.; Eyring, L. J. Solid State Chem. **1996**, 122, 53–58.

[18] Mohamed S. El-Genka,b,* Jean-Michel P. Tourniera, "USES OF LIQUID-METAL AND WATER HEAT PIPES IN SPACE REACTOR POWER SYSTEMS," Frontiers in Heat Pipes (FHP), 2, 013002 (2011)

[19] http://www.haynesintl.com/pdf/h3000.pdf

[20] http://www.industrialheating.com/articles/83843-molybdenum-and-tantalum-offer-competitive-edge-in-hostile-environments?v=preview

[21] Committee on Coatings National Materials Advisory Board Division of Engineering National Research Council, "High-Temperature Oxidation-Resistant Coatings," National Academy of Sciences / National Academy of Engineering, Washington, D.C. (1970).

[22] http://web.ornl.gov/info/reports/1960/3445600213043.pdf

[23] Romero V.J., 1994, "CIRCE2/DEKGEN2: A Software Package for Facilitated Optical Analysis of 3-D Distributed Solar Energy Concentrators – Theory and User Manual," SAND91-2238.

[24] Andraka, C.E., Diver, R.B., "Reflux Heat-Pipe Solar Receivers for Dish-Electric Systems," 1988, Proceedings of the 23rd Intersociety Energy Conversion Engineering Conference, Denver, CO.

[25] Diver, R.B., Andraka, C.E., Moreno, J.B., Adkins, D.R., and Moss, T.A., 1990, "Trends in Dish-Stirling Solar Receiver Designs," Proceedings of the 25th Intersociety Energy Conversion Engineering Conference, Reno, NV.

[26] Charles E. Andraka, Rich Diver, Doug Adkins, Scott Rawlinson, Patricia Cordeiro, Vern Dudley, and Tim Moss, 1993, "Testing of Stirling Engine Solar Reflux Heat-Pipe Receivers," Proceedings of the 28th Intersociety Energy Conversion Engineering Conference, Atlanta, GA.

[27] Meredig, B.; Wolverton, C. Phys. Rev. B, **2009,** 80, 245119.

[28] Bingjun Xu, Yashodhan Bhawe, and Mark E. Davis, "Low-temperature, manganese oxide-based, thermochemical water splitting cycle," PNAS, June 12, 2012 , vol. 109, no. 24, 9260-9264

[29] Pickens Plan, www.pickensplan.com

[30] Lee, A., Zinaman, O., and Logan, J., 2012, "Opportunities for Synergy Between Natural Gas and Renewable Energy in the Electric Power and Transportation Sectors," National Renewable Technology Laboratory NREL/TP-6A50-56324, Golden, CO.

[31] McQuillan, B.W., Brown, L.C., Besenbruch, G.E., Tolman, R., Cramer, T., Russ, B.E., Vermillion, B.A., Earl, B., Hsieh, T., Chen, Y., Kwan, K., Diver, R., Siegal, N., Weimer, A., Perkins, C., and Lewandowski, A., 2010, "High Efficiency Generation of Hydrogen Fuels Using Solar Thermal-Chemical Splitting of Water (Solar Thermo-Chemical Splitting for H2)," GA-A24972. Prepared under Solar Thermochemical Hydrogen Grant No. DE-FG36-03G013062 for the US Department of Energy and F03-STCH2-002 for the University of Nevada Las Vegas Research Foundation, General Atomics, San Diego, CA

[32] James E Miller, Mark D Allendorf, Richard B Diver, Lindsey R Evans, Nathan P Siegel, John N Stuecker, 2008, Metal Oxide Composites and Structures for Ultra-High Temperature Solar Thermochemical Cycles, Journal of Material Science, **43:4714-4728**.

[33] Meredig, B., Wolverton, C., 2009, "First-Principles Thermodynamic Framework for the Evaluation of Thermochemical H2O- or CO2-Splitting Materials," Physical Review B **80**, 245119.

[34] Brown L.C., Besenbruch G.E., Lentsch R.D., Schultz K.R., Funk J.F., Pickard P.S., Marshall, A.C., Showalter, S.K., 2003, "High Efficiency Generation of Hydrogen Fuels Using Nuclear Power," GA-A24285. Prepared under the Nuclear Energy Research Initiative Program for the US Department of Energy, General Atomics, San Diego, CA.

[35] Onuki, K., Shimizu, S., Nakajima, H., Ikezoe, Y., Sato, S., 1987, "Study of Catalytic Reduction of Methanol for Methane-Methanol Thermochemical Hydrogen Production Cycles," Int. J. Hydrogen Energy, Vol. 12, No. 8 pp 555-559.

[36] US. Patent 3,984,530, Dreyfuss, R.M., Hickman, R.G., 1975. "Methane-Methanol Cycle for the Thermochemical Production of Hydrogen."

[37] US. Patent 4,756,806, Krist, F.K., Serauskas, R.V., 1987, "Hybrid Thermoelectrochemical Synthesis of Gaseous Fuels from Water and Carbon Dioxide."

[38] Spiewak, I., Tyner, C.E., Langnickel, U., 1993, "Applications of Solar Reforming Technologies," SAND93-1959, Sandia National Laboratories, Albuquerque, NM.

[39] Steinfeld, A., 2005, "Solar Thermochemical Hydrogen Production – A Review," Solar Energy 78 (2005) 603-615.

[40] N.P.Siegel, J.E. Miller, I. Ermanoski, R.B. Diver, E.B. Stechel, 2013, "Factors Affecting the Efficiency of Solar Driven Metal Oxide Thermochemical Cycles," Ind. Eng. Chem. Res. 2013, 52, 3276−3286.

[41] Miller, J.E., 2007, "Initial Case for Splitting Carbon Dioxide to Carbon Monoxide and Oxygen," SAND2007-8012, Sandia National Laboratories, Albuquerque, NM.

[42] R. Palumbo, R.B. Diver, C. Larson, E.N Coker, J.E. Miller, J. Guertin, J. Schoer, M. Meyer, N.P. Siegel, 2012, "Solar Thermal Decoupled Water Electrolysis Process I: Proof of Concept," Chem. Eng. Sci. 84, pp. 372-380.

[43] Halley, J.W., Schofield, A., Berntson, B., 2012, "Use of Magnetite as Anode of Electrolysis of Water," Journal of Applied Physics **111**, 124911.

[44] Gas Technology Institute (GTI),"Methane to Methanol Fuel: A Low Temperature Process," http://arpa-e.energy.gov/?q=arpa-e-projects/efficient-natural-gas-methanol-conversion